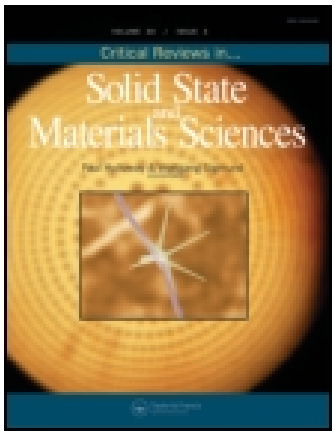

Critical Reviews in Solid State and Materials Sciences
Publication details, including instructions for authors and subscription information:
http://www.tandfonline.com/loi/bsms20

Radiation Damage in Metals

E. Friedland [a]
[a] Physics Department University of Pretoria 0002 Pretoria, South Africa
Published online: 24 Jun 2010.

To cite this article: E. Friedland (2001) Radiation Damage in Metals, Critical Reviews in Solid State and Materials Sciences, 26:2, 87-143, DOI: 10.1080/20014091104170

To link to this article: http://dx.doi.org/10.1080/20014091104170

Radiation Damage in Metals

E. Friedland
Physics Department
University of Pretoria
0002 Pretoria, South Africa

Table of Contents

1040-8436/00/$.50

I. Introduction

Interest in radiation damage started about fifty years ago when the first nuclear reactors were built. At that stage studies were mainly concerned with the change of material properties due to neutron irradiation, as this could influence safety aspects of the reactor design. With neutrons two types of defects are introduced into the material. Firstly, lattice atoms can be displaced by elastic collisions and secondly, impurity atoms are introduced into the material by nuclear reactions. This possibility to introduce point defects into lattices by particle irradiation makes it, of course, an attractive method for fundamental research on defect dynamics. Energetic electrons are especially useful for such studies. Because of the huge mass difference, they transfer a relatively small fraction of their energy to the lattice atoms, which makes them ideally suited for determining activation energies of simple point defects. In more recent times radiation effects in metals by heavy ions became an important research area, as ion implantation techniques are increasingly used in modern metallurgy to create new and useful surface properties like increased wear resistance and hardness. In the latter case large amounts of energy are released within relatively small volumes, producing extended defect structures by damage mechanism involving many particles.

Many of the basic mechanisms responsible for radiation damage were in principle already understood in the sixties and are discussed in depth in an excellent monograph by Thompson [1]. However, as radiation damage can only be treated rigorously by using many-body methods, a detailed picture of all aspects is only now slowly evolving, mainly because of the increasing availability of powerful computers.

II. Overview of Defect Mechanisms in Metals

A. Kinematics of Binary Collisions

A point defect is created in a binary collision if sufficient energy is transferred to an atom to displace it permanently from its lattice position. The energy transferred in an elastic collision depends on the masses of the particles involved and the impact parameter. Maximum energy T_{max} is transferred in a head-on collision and the accompanying momentum transfer is given by the relativistic expression

$$P_{max} = 2p\frac{M(\gamma m + M)}{m^2 + 2\gamma mM + M^2} \tag{1}$$

with γ the Lorentz factor. This reduces in the classical limit ($\gamma \to 1$) to

$$P_{max} = 2p\frac{M}{m + M}$$

and

$$T_{max} = \frac{4mM}{(m + M)^2}E \tag{2}$$

Here m and p refer to the mass and momentum of the bombarding particle with kinetic energy E, whilst M is the mass of the target atom, which is assumed to be at rest. For neutrons and ions up to an energy of a few MeV per nucleon the classical approximation is appropriate, while the relativistic expression must be used for energetic electrons. The corresponding fraction of energy transferred is

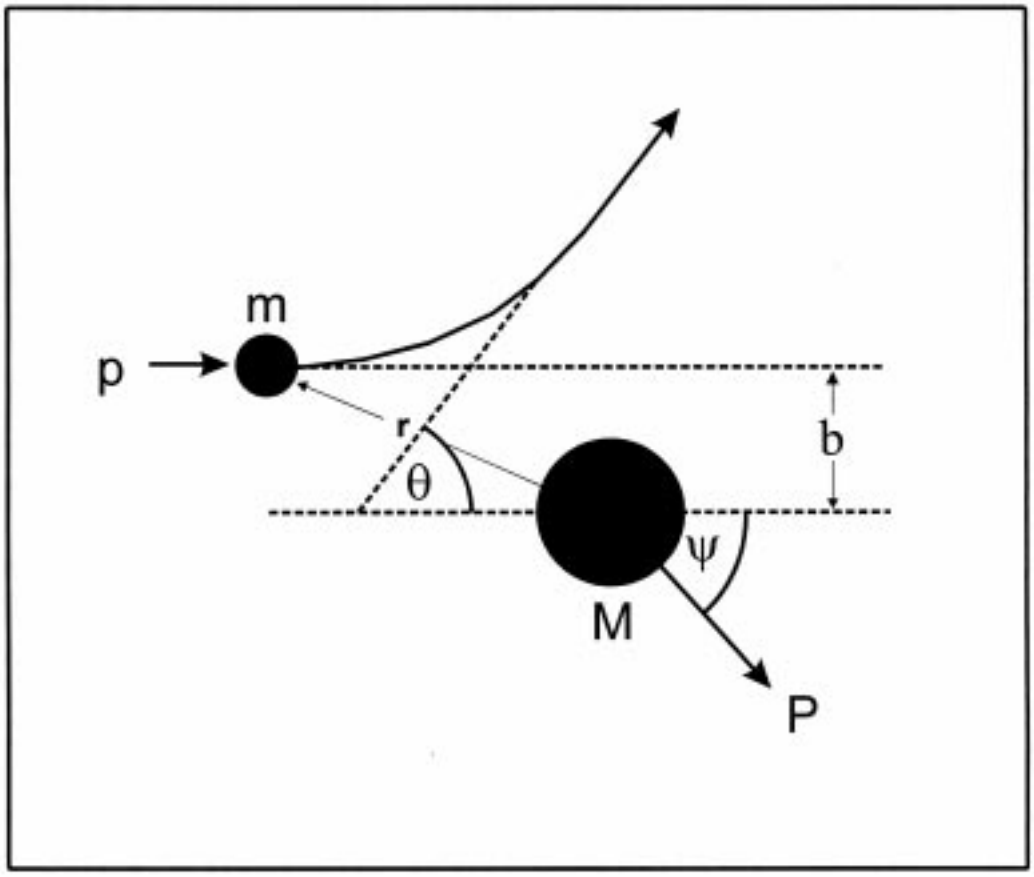

Figure 1: Binary collision of a particle *m* with a target atom *M* at rest in the laboratory system.

relatively small for large mass differences and reaches unity when the two masses are alike. However, one has to keep in mind, that most collisions occur with non-zero impact parameters. This leads to a reduced energy transfer

$$T = T_{max} cos^2 \psi \tag{3}$$

with ψ the scattering angle of the recoiling target atom. As the recoil angle, which is a function of the scattering potential, increases with impact parameter *b* (Fig. 1), the probability for collisions with low energy transfer is high. Many interactions with large impact parameters will therefore lead to sub-threshold energy transfers. Such events cannot create defects but will only excite phonons which can be responsible for radiation induced annealing effects.

B. Point Defect Stability

Many computer calculations have been performed to establish the configuration of stable point defects and the size and shape of the spontaneous recombination volume of a vacancy-interstitial pair. The first extensive numerical machine computations were performed for the *fcc* system of

copper by Gibson *et al* [2]. In these calculations a crystallite of approximately 500 atoms imbedded in an infinite perfect crystal was considered. The atoms of the crystallite were assumed to interact with each other by a two-body repulsive Born-Mayer-type potential, which was balanced by surface forces to simulate the binding energy, which in a metal is mainly due to the conduction electrons. Static calculations at zero point temperature showed that the nearest neighbours of a vacancy relax radially inward by approximately 3% of the equilibrium distance, while the second and more distant neighbours relax slightly outward. The stable configuration for an interstitial atom was found to be that of a symmetric dumbbell, sharing a lattice site along a <100> direction. The crowdion configuration, which is formed by inserting an interstitial atom along the <110> chain was found to be just unstable (Fig. 2). It decayed slowly by rotation into the <100> alignment to form the stable dumbbell configuration. Similar calculations were performed for the *bcc* system of α-iron [3, 4]. In this case a split interstitial in the <110> direction was found to be stable, while a metastable crowdion seems possible along the <111> direction [4]. This was confirmed by recent molecular dynamic simulations for *bcc* iron [5], showing that sufficiently high energy barriers exist between the two interstitial configurations to turn crowdions at 10 K into long-life metastable states. If placed in the stress field of either an edge dislocation or a large point defect cluster the energy levels are even inverted, making the crowdion configuration the ground state. Furthermore thermal excitation from dumbbell to crowdion states were predicted for isolated interstitial atoms at temperatures above 50 K. In *hcp* metals the situation is more complex, as a number of different interstitial configurations are possible. Calculations for a variety of *hcp* metals indicate that the stable configuration is either a basal interstitial midway between two octahedral sites or a dumbbell in the *c*-direction, depending on whether the ratio c/a is smaller or larger than the ideal value of $(8/3)^{1/2}$ [6]. A detailed analysis of experimental results by Frank [7] indicates furthermore the existence of a metastable non-basal crowdion. The stability and dynamical properties of static metastable crowdions in both cubic and hexagonal metals is the subject of a long and controversial debate, which has not yet been settled and will be briefly discussed in chapter IV-A.

A vacancy-interstitial pair will be stable if the distance between them is large enough to prevent spontaneous recombination due to the attractive force created by their mutual stress field. The minimum distance required to establish a stable Frenkel defect depends on the lattice structure and atomic potential. It is found to be strongly anisotropic with a relatively large separation of at least four lattice sites along the densely packed <110> rows in the *fcc* system and <111> rows in the *bcc* system. Smaller distances are possible in other directions. All close pairs within the boundaries of this recombination volume are unstable.

The preceding discussion of point defect stability does not take into account any thermal effects. At temperatures $T > 0$ K thermal vibrations of the lattice atoms can lead to migration of defects if sufficient energy is supplied to overcome the potential barrier between adjacent equilibrium positions. The jump rate ν depends on the migration activation energy E^M and is given by

$$\nu = \nu_0 exp(-\frac{E^M}{kT}) \tag{4}$$

with $\nu_0 \sim 10^{13}$ s^{-1} the Debye frequency. Typically migration energies in the order of 1.3 eV for vacancies and 0.15 eV for interstitials are predicted for *fcc* metals [8], with the migration energies for crowdions expected to be always significantly lower than for other interstitial configurations. From this it follows that interstitials in metals are mobile even at relatively low temperatures. During their motion through the lattice, point defects can be annihilated by their anti-defects or at the surface, be trapped at impurities and dislocations, or form less mobile defect clusters. The force between

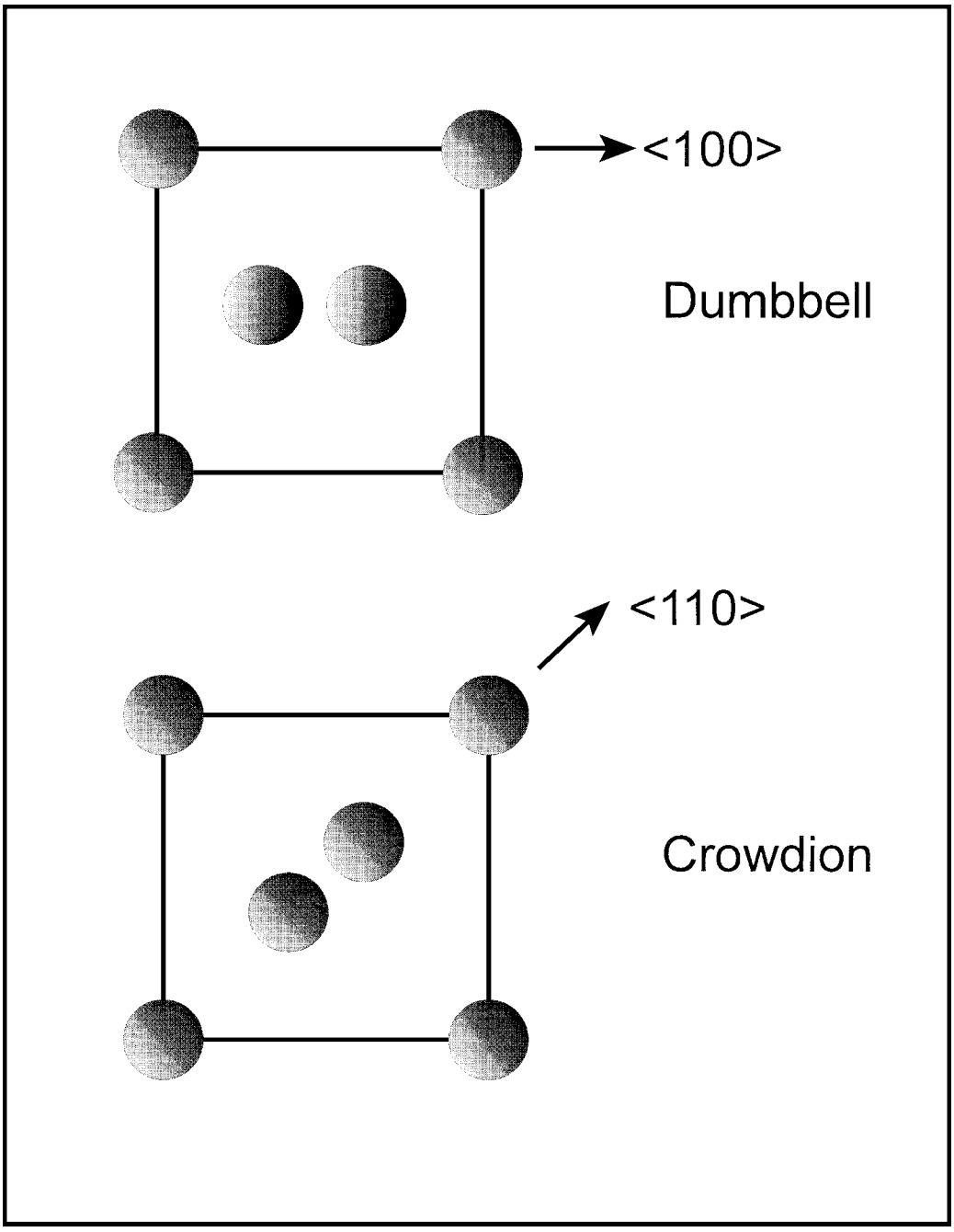

Figure 2: Schematic representation of dumbbell and crowdion configurations in the (100) plane of an *fcc* lattice.

two interstitials seems to be of the same order than between a vacancy-interstitial pair, while it is much smaller for di-vacancies. Binding energies E^B and migration energies E^M for small clusters in *fcc* and *bcc* lattices have been theoretically investigated assuming a Born-Meyer potential [2, 9], a Morse function [10] and a two-body central force interaction derived from elastic moduli [11]. Binding energies for interstitial clusters are high, while their migration energies are relatively low. For di-interstitials values of $E^B_{2I} \sim 1$ eV and $E^M_{2I} \sim 0.3$ eV are expected. The opposite trend is found for vacancy clusters, where binding is relatively weak and migration energies are high. Typical values for di-vacancies are $E^B_{2V} \sim 0.3$ eV and $E^M_{2V} \sim 0.9$ eV. For both type of clusters the binding and migration activation energies increase with cluster size. Experimental binding energies for some di-interstials are $E_{Fe} = 0.2$ eV [12], $E_{Cu} = 0.6$ eV and $E_{Ni} = 0.8$ eV [13]. The energetically favoured structures for higher order defect clusters are often planar configurations, representing vacancy or interstitial type dislocation loops. Stable interstitial clusters can be either sessile dumbbell or glissile crowdion agglomerates. Computer simulations [14] predict highly mobile interstitial clusters in α-iron. However, their highly anisotropic mobilities only permit one-dimensional migration along the close-packed <111> direction. The probability of changing migration direction to one of the other <111> directions has been investigated for small clusters ($2 \leq N \leq 4$) using a semi-empirical embedded-atom potential [15]. So far all mobile clusters in metals obtained by computer simulations are densely packed parallel crowdions having activation energies around 0.03 eV [16].

C. Displacement Energies

An atom will be displaced from its lattice position, if the transferred energy is larger than the sum of the formation energies [17, 18] of a vacancy ($E^F_V \sim 1$ eV) and an interstitial atom ($E^F_I \sim 4$ eV). However, the displacement energy E_d needed to move the interstitial outside the spontaneous recombination volume of its own vacancy is significantly larger than the reversible formation energy of a Frenkel defect. A first crude estimate of the displacement energy was made by Seitz [19], who suggested that it should be 4 to 5 times the sublimation energy. This proved to be a reasonable value for many metals. There are some obvious exceptions (e.g., Zn, Ag, Au) where this value is too low [20].

Because of the non-spherical shape of the spontaneous recombination volume and also as a result of the existence of certain lattice directions along which interstitials are transported easier over large distances than along other directions, the displacement energy E_d is strongly anisotropic. Computer simulations predict minima for the threshold energy surface along close-packed lattice directions. For *fcc* copper $E_d \sim 25$ eV along the <100> and <110> chains and $E_d \sim 85$ eV along the <111> chain were found [2], while for *bcc* iron threshold energies of ~ 17 eV for <100>, ~ 34 eV and ~ 38 eV for <111> chains and larger energies along other directions were obtained [3]. Analytical methods to construct threshold energy surfaces for cubic lattices have also been undertaken [21, 22, 23, 25]. In alloys each constituent element will have its own specific energy surface with maxima and minima not necessarily along the same crystallographic direction [24].

Empirical displacement energies E_d for metals were mainly obtained by measuring resistivity changes due to electron irradiation at low temperatures. Other methods used were diffuse X-ray scattering and high-voltage electron microscopy. By determining the minimum electron energy needed to introduce radiation damage, displacement energies can in principle be extracted. The shape of the threshold energy surface has been experimentally investigated for *fcc* metals [12, 26, 27, 28, 29, 30, 31, 32], *bcc* metals [32, 33, 34, 35, 36] and *hcp* metals [31, 37] by measuring damage rates as a function of energy and beam direction in thin foils. However, the analysis of experimental

data is not straight forward, as displacements at an angle ψ relative to the beam direction reduce the transferred energy by a factor $cos^2\psi$. The threshold energy for damage production along the beam direction is therefore not necessarily related to the displacement energy along this direction. If the displacement energy along the beam direction $E_d(0) > E_d(\psi)/cos^2\psi$ for any $\psi < \pi/2$, then an apparent threshold energy of $E_d(\psi)/cos^2(\psi)$ will be found. To determine the threshold energy profile, a complete set of measurements covering all fundamental lattice directions is needed, which must then be fitted simultaneously to a corresponding set of damage rate functions as discussed by Jung *et al* [29]. Fig 3 shows their results for copper and platinum together with the computer

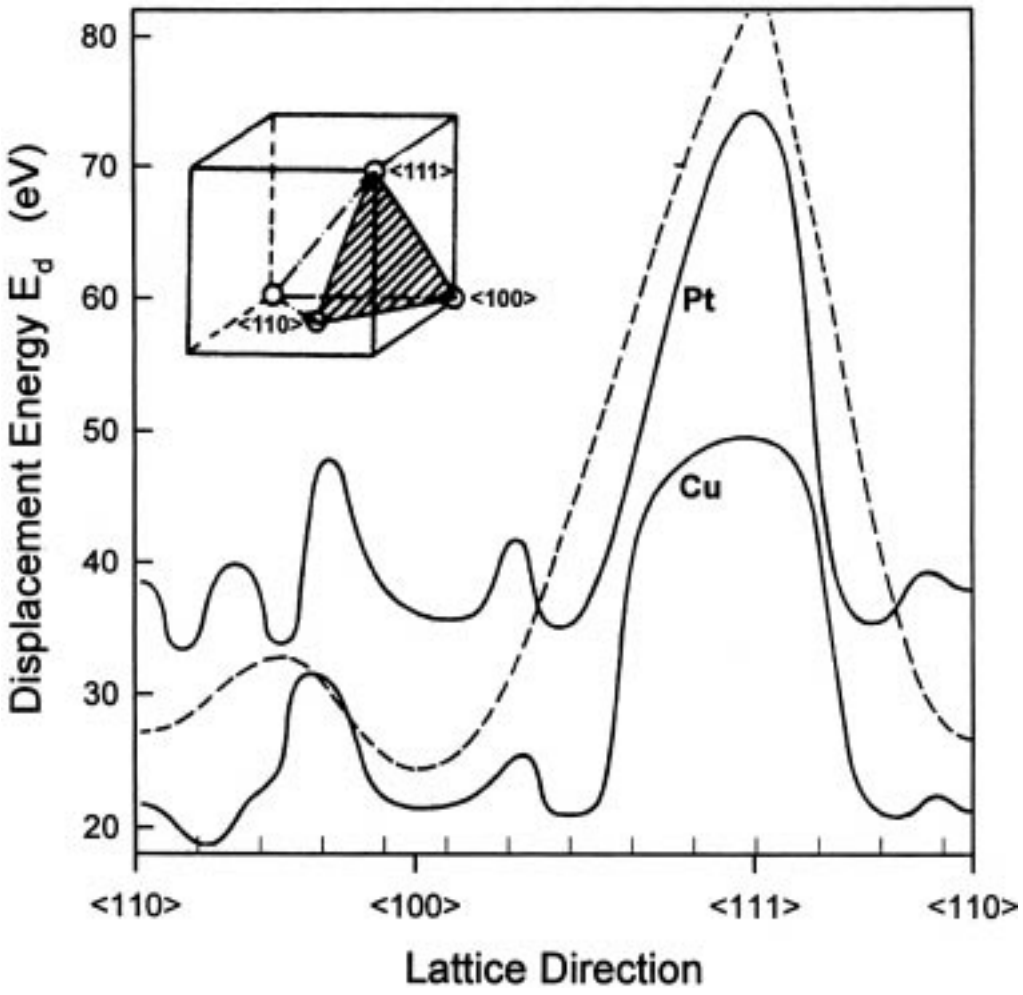

Figure 3: Experimental displacement energy contour of copper and platinum together with theoretical calculations depicted by a broken line. (From reference [29].)

calculations of Gibson *et al* [2] for the directions along the border of the fundamental triangle, which is shown as an inset. The main features of minima near the <110> and <100> directions as well as the maximum near the <111> direction is reproduced quite satisfactorily. Lowest displacement

energies in *fcc* metals are generally found for the <110> direction. For most *bcc* metals the lowest value is found along the <100> direction, but local minima are also found near the other two main crystallographic directions with appreciable higher values for intermediate directions. Results for *hcp* metals are variable but often show lowest displacement energies for the densely packed $<11\bar{2}0>$ row, an appreciably higher secondary minimum near the <0001> direction and much higher values for intermediate directions. A critical evaluation of displacement energy determinations up to 1977 is contained in Vajda's review paper [38].

D. Displacement Collision Sequences

The minima of the displacement energies along main crystallographic directions can be explained by the possibility of transporting energy and mass along close-packed atomic rows over relatively large distances. It was already noted in the late fifties by Silsbee [39] that focusing collisions cause dynamic crowdions to travel along those rows, creating interstitials at some distance from the primary knock-on atom [40]. Assuming hard-sphere binary collisions along an isolated atomic chain (Fig. 4), the ratio Λ for small recoil angles α of successive collisions is given by

$$\Lambda = \alpha_{i+1}/\alpha_i \sim D/2r_0 - 1 \tag{5}$$

with D the distance between the centres of adjacent atoms and r_0 the atomic radius. Recoil angles

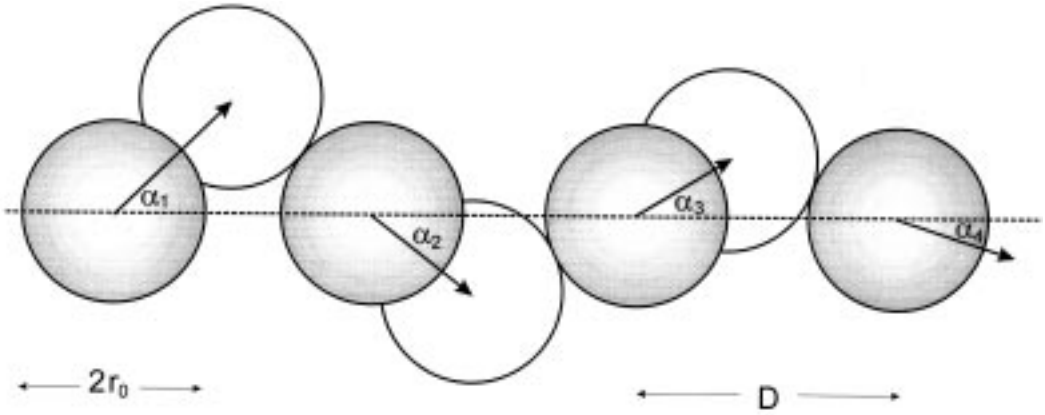

Figure 4: Schematic illustration of focusing collisions along an isolated atomic row according to reference [39].

will decrease and focusing will occur if $D < 4r_0$. A necessary condition is therefore a close-packed row with relatively large interaction radii. As the hard sphere radius r_0 is effectively given by the energy dependent distance of closest approach, it follows that focusing is only expected at rather low recoil energies. However, in a real crystal the atomic rows are not isolated and neighbouring chains will influence the motion of recoiling atoms. This relaxes the above condition to some extend and leads to assisted focusing along less densely packed crystallographic orientations [41, 42]. It also limits the length of focusons because energy is transferred to atoms of neighbouring chains. Further energy losses are due to thermal and isotopic effects. Conservative estimates put the typical length of a focuson at about 10 atomic distances. Assuming a Born-Mayer-type potential $V(r) = Aexp(-r/a)$

and taking $2r_0$ as the distance of closest approach in a head-on collision, the maximum focusing energy for hard-sphere scattering along an isolated chain is found to be

$$E_f = 2Aexp(-D/2a) \tag{6}$$

The hard-sphere approach does not take into account any dependence of r_0 on the impact parameter b and cuts off all contributions for $b > 2r_0$. This approximation overestimates focusing and modified expressions for non-rigid collisions are discussed in references [43, 44]. Applying these corrections, a focusing energy of 35 eV is obtained for the close-packed <110> chain in copper [45]. This compares quite well with the value of 30 eV obtained by computer simulations [2], which also showed assisted focussing along the less dense <100> chains at energies below 40 eV. In α-iron focusing is predicted by computer simulations below 28 eV along the <111> chain and below 18 eV along the <100> chain [3]. For *hcp* metals focusons are expected along the $<11\bar{2}0>$ direction.

E. Collision Cascades

If a lattice atom is struck by an ion or fast neutron, the transferred recoil energy is often large enough to enable the displaced atom to displace further lattice atoms, leading to a random multiplication process. The energy distribution $\Pi(T) = TP(T)$ for primary knock-on atoms (PKA) is strongly biased towards small recoil energies T as is illustrated in Fig. 5 for a variety of ions impinging on a silver target [46]. The probability for them to be involved in secondary elastic collisions is therefore quite high. As furthermore the conditions for energy transfer is optimal between atoms with equal masses, the energy of the PKA will be relatively fast distributed between many atoms in a small volume. After $t \sim 10^{-13}$ s the collisional stage comes to an end, when the kinetic energies of all moving atoms in the cascade region have dropped below the displacement energy E_d. Typically less than 20% of the original PKA energy has than been used up in defect creation. At this stage the defect configuration consists of a depleted core zone with an average vacancy concentration of approximately 10%. The interstial atoms have mainly been transported to the peripheral region by displacement collision sequences; those left in the core region have a very small survival probabilty due to the high local vacancy density.

The relatively large fraction of the PKA's kinetic energy left in the cascade zone will lead to local heating, starting the second stage of cascade evolution, which is often referred to as the thermal spike phase. Whether any significant rearrangement of the depleted zone's defect structure occurs during this stage depends largely on its lifetime. This is primarily a function of the cacade size, the thermodynamic properties of the material within and without the cascade zone as well as the ambient temperature of the surrounding undisturbed lattice. First estimates by Seitz and Koehler [47] led to lifetimes of $t \sim 10^{-12}$ s, which is generally assumed to be short enough to prevent appreciable defect rearrangement by vacancy migration. That this is not necessarily always the case has been shown by molecular dynamic simulation studies of the thermal stage in copper [48, 49]. For small cascade sizes (10 - 20 A) and fast cooling rates similar lifetimes as mentioned above were obtained, resulting in an overheated solid body without significant modification of the defect structure. However, for larger cascades (50 - 100 A) and slow cooling rates lifetimes an order of magnitude longer were calculated. In this case local melting and recrystallization occurs with significant changes of the defect configuration. As a result of the large temperature gradient within the cascade zone, vacancies move to the core region forming large vacancy clusters or voids. Further studies of void annealing make its transformation during this stage into a vacancy type dislocation loop a distinct possibility.

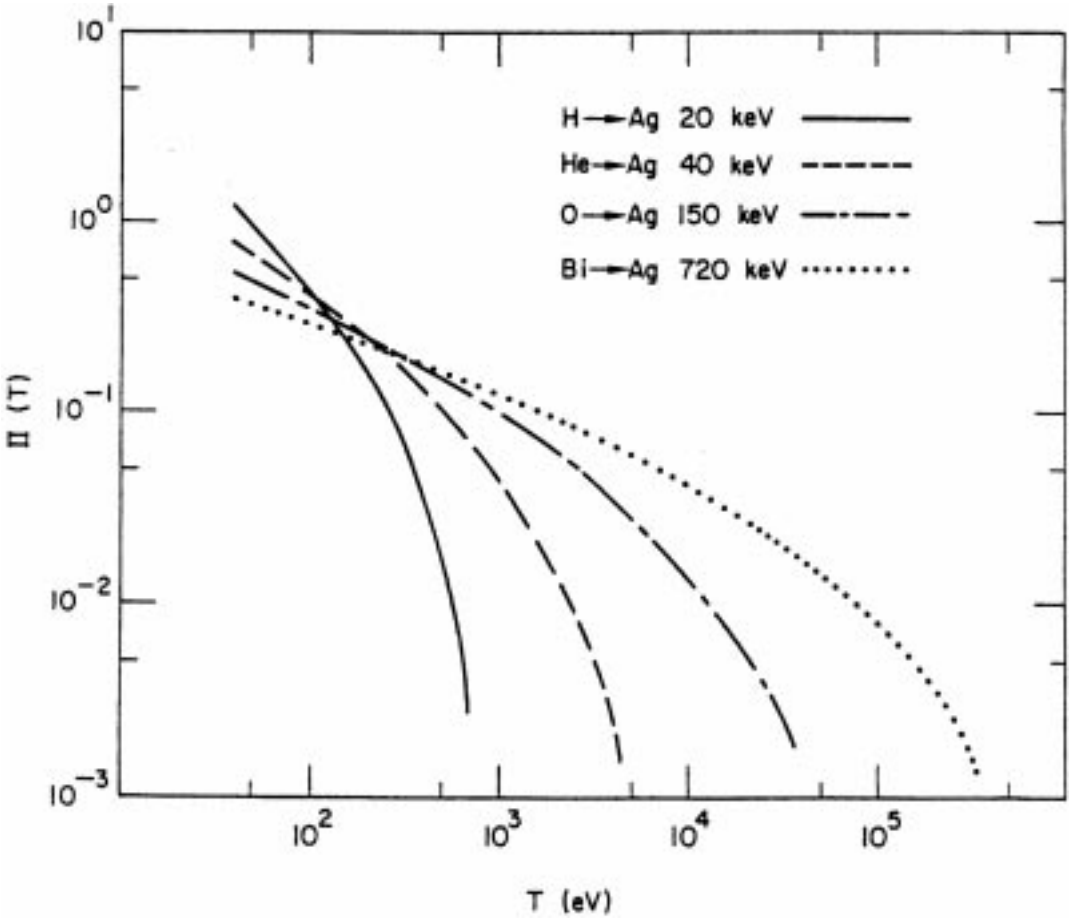

Figure 5: Energy spectrum of primary recoil atoms calculated for different ions bombarding a silver target. (From reference [46].)

The final and third stage in cascade evolution is the relaxation phase, lasting up to 10^{-7} s, when defects mobile at ambient temperatures either escape from the cascade region or transform to lower energy configurations. At room temperature it is therefore expected that during this phase all mono-interstials have either been annihilated or have formed interstitial clusters, while not much will change for implantations at $T_i < 10$ K.

The defect density in a cascade depends on the mass of the lattice atoms. For a given PKA energy rather open defect structures are expected in light targets, while a dense damage network is typically for heavy target materials. The differential cross section $\kappa(E, T)$ for transferring recoil energy T to a target atom from an ion with energy E can be calculated for a given interaction potential. If furthermore the damage function $g(T)$ is defined as the number of defects produced by a PKA with recoil energy T, then the damage cross section is given by:

$$\sigma_D(E) = \int_0^{T_{max}} g(T)\kappa(E, T)dT \tag{7}$$

and the damage rate in displacements per atom (dpa) and per unit time by:

$$G = \sigma_D(E)\phi \tag{8}$$

with ϕ the ion flux. The atomic potentials are well known and $\kappa(E, T)$ can be calculated quite accurately. This is unfortunately not the case for the damage function $g(T)$. A first estimate of the damage function was obtained by Kinchin and Pease [50], assuming hard sphere scattering:

$$\begin{array}{rcll} & = & 0 & (T < E_d) \\ g(T) & = & 1 & (E_d < T < 2E_d) \\ & = & kT/(2E_d) & (T > 2E_d) \end{array} \tag{9}$$

The first of these three equations simply states that recoil energies below the displacement energy E_d will not result in any defect, because the struck atom cannot escape from its position. The other two equations can be intuitively understood by realizing that a moving atom needs at least twice the displacement energy to displace an atom from its position and still retain enough energy to escape from the created vacancy. If this is not the case, only replacement takes place without formation of an additional defect. The factor k in the third equation was originally taken as unity. But in the modified version, which corrects for the somewhat unrealistic hard sphere approximation [51, 52, 53], a value of 0.8 is generally used. The above treatment does not take into account the possibility of point defect annihilation by their anti-defects in the dense damage structure of the cascade core. It also neglects inelastic scattering, which becomes an important energy-loss mechanism at higher energies. In order to correct for the latter, an ionization energy E_C is sometimes introduced [54] to replace T in the third equation whenever $T > E_C$. This limits the number of displacement collisions above a sharply defined transition energy, which is a rather artificial procedure to describe the continuously increasing importance of electronic excitation and ionization at higher energies. A more satisfying approach by Norgett, *et al.* [53] replaces T by $T' = T - < Q >$ with <Q> the average electronic energy loss in the cascade:

$$g(T) = \frac{0.8(T - < Q >)}{2E_d} \tag{10}$$

However, despite these refinements of the theory, other simplifications like the neglection of annealing effects during the late stages of cascade evolution and the possible melting of the cascade core, lead generally to an overestimation of the damage function by the Kinchin-Pease approach. This becomes more serious with increasing ion mass.

The damage efficiency ξ, defined as the ratio of the experimentally observed number of defects and that predicted by the modified Kinchin-Pease formula (eq. 9), has been determined for a variety of ion-target combinations and energies [46, 55, 56]. The results indicate that the efficiency decreases monotoneously from approximately unity for recoil energies just above the threshold energy, reaching an almost constant value of $\xi \sim 0.3$ for energies above a few keV. Relatively good predictions of the damage function are obtained with an empirical power law [16]

$$g(T) = AT^m \tag{11}$$

with T given in keV and constants $A \sim 5$ and $m \sim 0.75$, depending weakly on material and temperature. Data obtained from molecular dynamic simulations for some pure metals and an alloy at 100 K agree very well with this equation as illustrated in Fig. 6. Also shown is the prediction

by the modified Kinchin-Pease model, including the correction for inelastic scattering (eq. 10). The results show a decreasing Frenkel-pair production efficiency with increasing PKA energy. The above equation does not include intersite defects in the ordered alloy that become more important at higher energies and can be described by a similar power law. For higher crystal temperatures the efficiency for Frenkel-pair production gradually decreases, while the number of created antisite defects in ordered alloys increases.

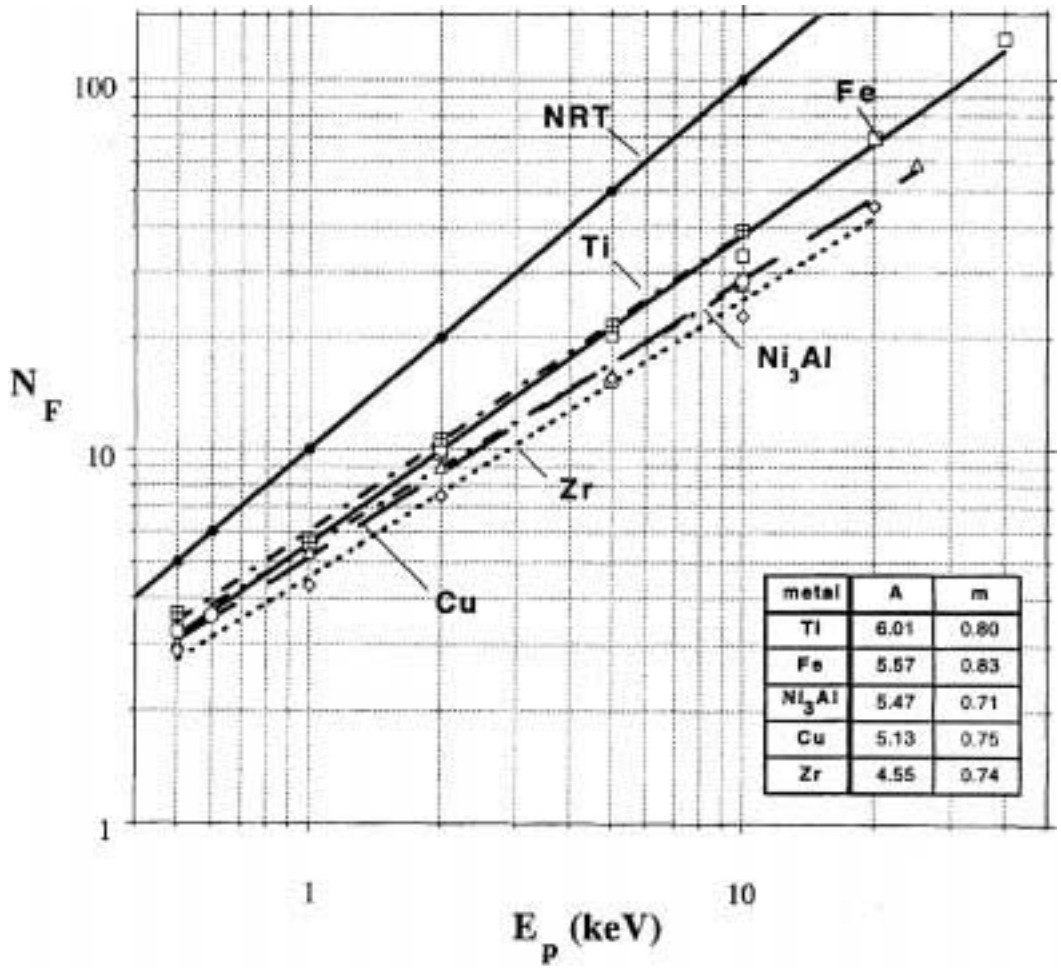

Figure 6: Comparison of the Frenkel-defect production as a function of PKA energy T determined by computer simulations and equation 11. The solid line marked NRT shows the result of equation 10. (From reference [16].)

A satisfactory theoretical treatment of the collision cascade is difficult because the processes involved are non-linear many-body interactions. However, the initial phase, when only a few particles are in motion and energies are relatively high, can quite satisfactorily be treated by assuming isolated binary collisions with stationary atoms only. Beeler [57] applied this method to calculate displacement efficiencies for α-iron, copper and tungsten. The results show displacement efficien-

cies to be a decreasing function of the PKA energy, in contrast to the constant value predicted by the Kinchin-Pease model. According to these calculations energy dependence is predominantly caused by point defect annihilation as a result of defect interference, while channeling plays only a minor role. This approach is also applied in the widely used computer code MARLOWE [58], which simulates displacement cascades in crystalline solids by assuming a conservative central repulsive force acting between atoms. Either a Born-Mayer potential or the Moliére approximation of the screened Coulomb potential is used. Uncorrelated recombination of point defects, which should be an important effect in the highly disturbed core region of the cascade, is taken into account by applying a realistic vacancy-interstitial separation criterion. The number of stable Frenkel defects obtained by this procedure is significantly reduced if compared with the modified Kinchin-Pease estimate; but the calculated damage efficiency is still approximately twice as large as experimentally found [59]. A modified binary collision approximation algorithm [60], aiming at a better ordering of the collisions in time, reduces this discrepancy to some extent, especially for heavy target atoms.

All binary collision models predict a vacancy rich core with the interstitials moving to the peripheral region of the cascade. Monte Carlo calculations [61] have shown that about 80% of the interstitials escape from the cascade, some of them forming small clusters ($2 \leq N \leq 4$). The remaining 20% interstitial atoms are annihilated in the core region. This is in qualitative agreement with experimental results and is obviously a development already taking place during the early stages of cascade evolution. The extremely popular TRIM code [62], which assumes an amorphous solid, is based on the binary collision model. In order to achieve high computing efficiency and speed, it makes use of a randomized impact parameter distribution and a simplified procedure to select free flight path lengths between individual collisions. However, as the damage function is calculated by means of the modified Kinchin-Pease formula, allowing for electronic energy losses only, it tends to overestimate the number of point defects.

Realistic values of the damage function have up to now only be obtained by molecular dynamic simulations, which follow cascade development from the initial ballistic phase into the final stage when the affected region has been completely thermalized. These calculations proceed in real time by simultaneously solving Newton's equations of motion for all atoms involved, enforcing suitable boundary conditions to ensure the continued cohesion of the crystallite. Non-linear effects due to collisions between moving particles and the changing target structure are therefore largely taken into account. The large volume of computational steps, however, make molecular dynamic simulations extremely slow compared with binary collision calculations. Only a limited number of individual cascades can be investigated, leading to results, which might not always be statistically representative. The respective strengths and weaknesses of these two different approaches are critically discussed in review articles by Andersen [63] and Smith and Webb [64]. The first molecular dynamic calculations were limited by available computing power to energies of a few hundred electron volts [2, 3], which is not sufficient for cascade development and was therefore only used to investigate relatively simple defect configurations. However, with modern computers that can analyze crystallites containing more than 10^5 atoms, PKA energies of up to 50 keV can be treated [65]. Molecular dynamic simulations of displacement cascades with energies of a few keV indicate that local melting occurs in the central core. The lifetime of this molten state is of the order of several picoseconds, leading to large scale atomic mixing in this region. Most of the Frenkel pairs created within this region during the early ballistic phase recombine, a process which had already been predicted by Brinkman more than forty years ago [66]. Only those interstitials survive, which have been transported out of this region by replacement collision sequences, while the remaining vacancies tend to form clusters in the core

region. The final damage function is therefore mainly determined by the size of the thermal spike region and the average length of replacement collision sequences. Molecular dynamic simulations [67] predict defect efficiencies in copper of $\xi \sim 0.3$ for a 5 keV cascade in reasonable agreement with experimental results [55]. However, the experimentally observed formation of vacancy dislocation loops, which are assumed to be the result of cluster collapse, has not been reproduced. Furthermore, as the density during the thermal spike phase is considerably lower in the core region than in the surrounding material, severe stress gradients are generated in the peripheral zone. This might lead to secondary damage mechanisms beyond the cascade region, which is not accounted for by standard molecular dynamic simulations.

To describe the final stage of the collision cascade, when the initial recoil energy of the PKA has been distributed between many particles, classical heat transport calculations combined with chemical rate theory has been employed as a first approximation [68]. However, because of the spatially inhomogeneous energy distribution generally encountered in collision cascades and the anisotropic character of most solids, only qualitative information can be expected from such a treatment. A different approach combines binary collision calculations with classical quenching dynamics to model the relaxation phase [69], which, however, does not take into account the thermally enhanced recovery of the cascade region. Recently the evolution of defect structures during the relaxation phase has been modeled by a hierarchical combination of molecular dynamic and kinetic Monte Carlo methods [70, 71].

F. Void and Bubble Formation

The formation of non-planar vacancy agglomerates are observed in most metals and alloys after irradiation with high fluences of energetic neutrons [72, 73, 74, 75] or heavy ions at a temperature range of $0.3\ T_m \gtrsim T_i \gtrsim 0.6\ T_m$, where T_m is the absolute melting temperature. Formation of these defects always leads to swelling and has therefore important consequences regarding the mechanical properties of materials. An excellent review on void formation in irradiated metals has been published by Norris [76, 77].

In the case of fast neutrons voids normally start to occur at doses above 10^{19} n cm^{-2}, which corresponds to a displacement dose above 10^{-2} dpa. Void formation has not been observed after high energy electron irradiation of pure annealed metals, although void growth in the vicinity of dislocations occurs in samples which previously have been bombarded with heavy ions [78, 79, 80]. Voids after electron irradiation were also observed in samples containing oxygen impurities [81]. Obviously, suitable nucleation centres are prerequisites for void formation that under favourable conditions can subsequently grow into larger defect structures by vacancy capture. Nucleation seems to take place either near gas atoms, which prevent the collapse of vacancy clusters into dislocation loops, or at regions of super-saturated vacancy densities as found in the core region of collision cascades.

Energy considerations [82] indicate that in *fcc* metals voids should be the favoured defect configuration whenever the ratio of surface free energy to stacking fault energy $\gamma / \Gamma \lesssim 10$, while for larger ratios stacking fault tetrahedra are the preferred vacancy type defects. One would therefore expect that voids should be the most stable vacancy cluster in many metals. However, at low implantation temperatures faulted and unfaulted vacancy dislocation loops are generally observed with voids only appearing at higher temperatures [83]; indicating that defect kinetics plays a decisive role. Apparently, conditions conducive for void formation are sufficiently high vacancy mobilities combined with the presence of biased sinks for interstitials, leading to an oversupply of mobile vacancies. The

first condition is satisfied at an irradiation temperature of $T_i \gtrsim 0.3\ T_m$, while the last mentioned condition is the reason why voids only appear after high dose irradiation. This normally leads in metals to a dense dislocation network which serves as an efficient trap for interstitials. Without an excess of vacancies, voids could not grow and those already existing would shrink due to the preferential absorption of interstials. The fact that voids do not develop at irradiation temperatures $T_i \gtrsim 0.6\ T_m$ is due to an increased emission probability of vacancies from voids combined with a more efficient radiation-induced annealing effect, which reduces the dislocation density.

Gas-filled bubbles are often observed after high-dose irradiation with inert gas ions. This phenomenon is of great technological importance to the nuclear industry because of the high doses of helium ions occurring as transmutation products in fission reactors and fusion facilities. Helium bubbles can cause metal embrittlement in structural components and may furthermore result in surface blistering and exfoliation. A great deal of research has therefore been done on helium in metals, much of which was reported at a topical symposium in Jülich [84] and was previously reviewed by Donnelly [85].

Bubble formation does not depend on mobile vacancies and can, unlike voids, be observed at relatively low temperatures. It is assumed that normally bubbles are initiated by consecutive capture of implanted gas atoms I by a vacancy V, leading to the formation of a defect-impurity complex $V I_n$. When n reaches a critical number, the stress induced in the surrounding lattice can be reduced by the emission of an interstitial atom, which in turn allows the capture of more impurity atoms. Repetitions of this process eventually results in bubbles consisting of a number of vacancies filled with many gas atoms. At higher temperatures bubble formation can also proceed by agglomeration of mobile impurity-vacancy complexes [86]. Furthermore, the initial nucleation process can occur by a self-trapping mechanism, which does not depend on the availability of a vacancy [87]. In this case the vacancy is supplied by the spontaneous creation of a Frenkel pair in the stress field of a small cluster of interstitial impurity atoms. At high implantation temperatures ($T_i \gtrsim 0.5\ T_m$), when abundant mobile vacancies are available, the bubbles will be in thermal equilibrium with the surrounding lattice and their gas pressure is approximately balanced by the surface tension $2\gamma/r$. For typical bubble sizes this pressure is extremely high, leading to atomic densities far above that of the liquid phase. For example, a pressure of about 10 GPa has been estimated for a helium bubble with a radius of $r \sim 1$ nm in a nickel lattice [88]. Even higher pressures occur at low implantation temperatures, when bubbles are formed by athermal processes. This is expected to occur at a temperature range below $0.15\ T_m$, where self-interstitials and gas atoms are sufficiently mobile but vacancies are not [89]. If the supply of gas atoms is maintained, the pressure will eventually exceed the stability limit $p \sim (2\gamma + \mu b)/r$, where μ is the shear modulus of the matrix material and b the magnitude of the Burgers vector of dislocation loops. The accompanying stress field will then lead to further bubble growth by the emission of interstitial dislocation loops [90]. A process generally referred to as loop punching. As this mechanism is energetically more favourable than the emission of single interstitials, it will be the preferred athermal growth process for bubbles having surpassed a critical size. Tables of theoretical values for the expected pressure in helium bubbles for thermal equilibrium and athermal growth conditions are given in reference [85] for a variety of metals and bubble sizes. At the extremely high pressures calculated, no gas phases are expected for any of the rare gases. This is in accordance with experimental investigations, which for example revealed solid phases for argon and xenon and a liquid phase for neon in overpressurized bubbles after room temperature implantations into aluminum single crystals [91].

III. Stopping of Particles in Matter

A. Stopping of Electrons

Energetic electrons are losing energy in matter by inelastic interactions with target electrons, radiative processes and elastic collisions with target atoms. At energies below a few MeV atomic excitation and ionization is by far the most important stopping process, while emittance of bremsstrahlung becomes the dominant energy loss mechanism above an energy of $E \sim 1600mc^2/Z$ [92]. The energy lost by inelastic electron scattering will eventually be transformed by the electron-phonon interaction into heat, which might lead to annealing effects. With very intense electron beams even surface melting is possible. Displacement of target atoms can only be achieved by elastic scattering of the electrons by the Coulomb potential of the nuclear charge Z. The differential cross section for such interactions as a function of the atomic recoil angle ψ is approximately given by [93]:

$$\frac{d\sigma}{d\Omega} = (\frac{Ze^2}{mc^2})^2 \frac{(1-\beta^2)}{\beta^4 cos^3\psi}[1 - \beta^2 cos^2\psi + \frac{\pi Ze^2\beta}{hc} cos\psi(1 - cos\psi)] \tag{12}$$

with β the ratio of the electron velocity and the velocity of light. The cross section increases strongly with recoil angle, favouring forward scattering of electrons with small energy transfers to lattice atoms. Therefore electron irradiation leads mainly to the creation of isolated Frenkel pairs.

B. Stopping of Ions

Ions lose energy by elastic atomic collisions, which might displace a lattice atom, and by inelastic collisions with electrons. In metals the inelastic electronic collisions will either excite shell electrons into the conduction band or heat the electron gas. Except for very high electronic energy loss values ($|dE/dx|_e \gtrsim$ 10 keV/nm) neither of these processes leads to radiation damage, as the excess energy contained in the Bloch electron states will be quickly distributed within the electron gas and will eventually be transformed into thermal energy by the electron-phonon interaction. For charged particles at high velocities, energy loss is dominated by such inelastic electronic processes, while atomic collisions are only important at relatively low ion velocities.

The relative importance of electronic and nuclear stopping at a particular energy depends on the ion-target combination and can best be expressed as a function of the dimensionless reduced energy ϵ and reduced range ρ:

$$\epsilon = E\frac{aM}{zZe^2(m+M)} \tag{13}$$

$$\rho = 4\pi RNa^2\frac{mM}{(m+M)^2} \tag{14}$$

with E the ion energy, a the Thomas-Fermi screening radius, zZe^2 the charge product of the ion and target nucleus, R the range and N the atomic target density. By introducing the dimensionless quantity $t = \epsilon^2 T/T_{max}$, Lindhard *et al* [94] obtained for nuclear stopping the universal form

$$s_n = -\frac{d\epsilon}{d\rho} = \frac{1}{\epsilon}\int_0^\epsilon f(t^{1/2})d(t^{1/2}) \tag{15}$$

which is independent of the ion-target combination. The function $f(t^{1/2})$ depends on the form of the screened potential. Electronic stopping at low ion velocities v has been treated by Lindhard and Scharff [95]. It assumes a particularly simple form in reduced units for $v < v_0 z^{2/3}$:

$$s_e = -\frac{d\epsilon}{d\rho} = k\epsilon^{1/2} \tag{16}$$

with v_0 the Bohr velocity. However, this does not lead to universal stopping powers, as k depends on the ion-target combination. Electronic stopping reaches a maximum at $v \sim v_0 z^{2/3}$ which corresponds approximately to $\epsilon \sim 10^3$. At higher energies electronic stopping is described by the Bethe-Bloch formalism [96, 97] in terms of the stopping number L defined by:

$$-\frac{dE}{dx} = \frac{4\pi z^2 e^4}{mv^2} NZL. \tag{17}$$

For a review of ion stopping theory the reader is referred to references [62, 98, 99, 100, 101].

Nuclear and electronic stopping powers are plotted in Fig. 7 for the reduced energy range $0.01 < \epsilon < 100$. Nuclear stopping, which reaches a maximum at $\epsilon \sim 0.3$, has been computed by assuming a Thomas-Fermi potential while electronic stopping was calculated by using equation 16 for rare gas ions in a copper target. As only atomic collisions are responsible for defect creation in metals at low and medium energies, nuclear stopping powers determine to a large extend the radiation damage density. Fig. 8, which shows the stopping powers of Fig. 7 in practical units, illustrates the shift of the maximum of nuclear stopping to higher energies and its simultaneous growth with increasing ion charge and mass.

The stopping of fast light ions is mainly determined by a very large number of minute energy transfers due to forward inelastic scattering. The statistical fluctuations of the total energy-losses suffered by individual particles are therefore relatively small. After penetrating matter, the energy distribution of an initially mono-energetic ion beam has an approximately gaussian shape with a straggling width increasing roughly proportional with the square root of the total energy loss. For energies below the Coulomb barrier, which is typically for most radiation damage applications, particles are only removed from the beam by large angle scattering events. For higher energies, nuclear reactions can occur; but their contributions to the total interaction cross section is negligible, leaving the beam intensity practically constant until eventually the ion velocities are so far reduced to enter the final stage of almost pure nuclear stopping.

C. Stopping of Neutrons

In contrast to charged particles, which lose energy during their passage through matter by long-range Coulomb interactions, neutrons interact via the short-range nuclear potential. This interaction leads either to scattering events or nuclear reactions. Scattering results in energy-loss, while nuclear reactions attenuate the neutron beam intensity. Because of the relatively small interaction cross-section of fast neutrons with the nuclear potential, some of them can penetrate quite deeply into matter without losing any energy. The energy spectrum as a function of target depth will therefore exhibit an increasing fraction of low energy neutrons together with a decreasing component of neutrons with the original energy. After penetration of a layer thickness x the intensity of this latter component is given by:

$$I(x) = I_0 exp(-\sigma_t N x) \tag{18}$$

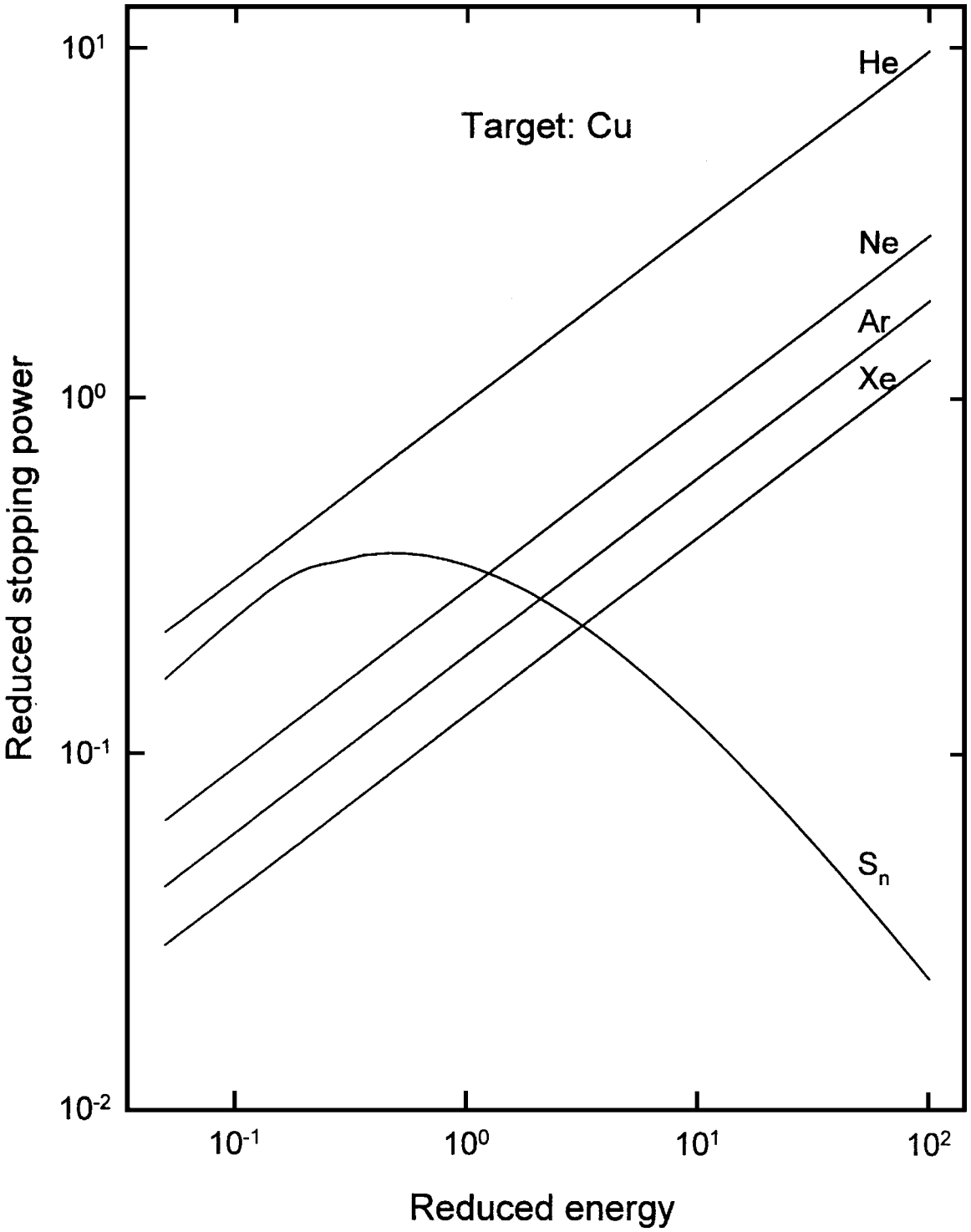

Figure 7: Nuclear stopping power as a function of reduced energy together with the electronic stopping powers for rare gases in copper.

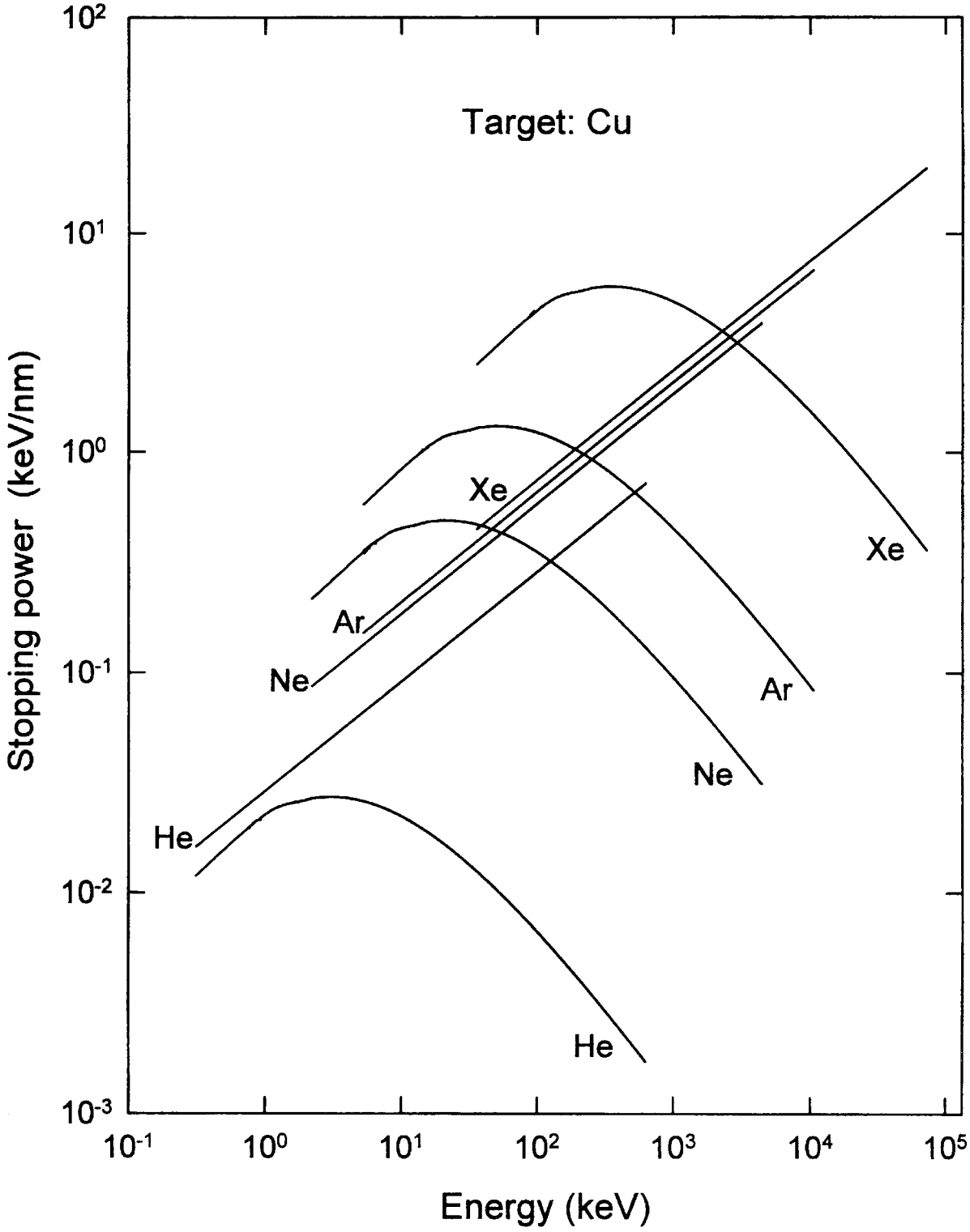

Figure 8: Nuclear and electronic stopping powers for rare gases in copper.

with I_0 the initial neutron beam intensity and $\sigma_t(E) = \sigma_s(E) + \sigma_r(E)$ the energy dependent total interaction cross section. The scattering cross section σ_s includes elastic and inelastic contributions, while the reaction cross section σ_r includes capture, fission and other nuclear reactions.

At relatively low energies, total cross sections often exhibit strong and sharp resonances, which depend on the internal structure of the nucleus. Although cross sections vary strongly for different target atoms, the average cross section for neutron capture shows a $1/v$ relationship for energies up to approximately 100 keV, with v the neutron velocity. The average behaviour of the elastic scattering cross section up to an energy of approximately 2 MeV can be qualitatively described by hard-sphere scattering, which is dominated by the isotropic s-wave contribution at neutron energies up to approximately 100 keV. The mean energy transferred to the recoiling nucleus is relatively high. At higher neutron energies higher order partial waves become important, leading to pronounced forward peaking of the differential scattering cross section (Fig. 9) with a corresponding decrease of high energy recoils. At energies above 2 MeV an increasing number of possible reaction channels, including inelastic scattering events, have to be taken into account and average elastic cross sections can only be described by a Woods-Saxon type optical potential [102].

If the total cross section is dominated by elastic scattering, which is usually the case in typical radiation damage experiments with fast neutrons, energy loss can be approximated [54] by:

$$-\frac{dE}{dx} \sim \frac{2N\sigma_t}{M} E \tag{19}$$

leading to typical ranges of a few centimeters for 100 keV neutrons.

IV. Defect Structures in Metals Due to Particle Bombardment

A. Radiation Damage with Electrons

Irradiation of metals with electrons at energies above the displacement threshold were extensively used in early studies to obtain information on simple point defect creation and their interactions with each other. The primary defect created by a fast electron is a Frenkel defect, i.e. a vacancy-interstitial pair. As interstitial atoms may have rather low migration energies, measurements were performed at low temperatures, typically at 10 K.

Defect densities were normally determined by electrical resistivity measurements. Information on the type of defects present and the evolution of the finite damage structure is obtained by annealing curves and by observing the time dependence of the electrical resistivity recovery. However, interpretation of electrical resistivity change $\Delta\rho$ must be treated with care as the contribution of interstitials in trapped or cluster configurations need not be the same as in a Frenkel pair. Furthermore, the order of the rate equation is only approximately constant for a given annealing mechanism.

Five main annealing stages [105], which in most cases exhibit substages, are generally observed in metals (Fig. 10) and are interpreted as being due to the recovery of different defect types. An excellent review of the results for *fcc* metals is given by Schilling *et al.* [106] and for *hcp* metals by Frank [7]. Although general consensus has been reached on most aspects of the mechanisms responsible for the different annealing stages and substages, there still rages an over 30 year old controversy about the question whether only one or two different interstitial configurations are involved. The one-interstitial model assumes that only the dumbbell configuration needs to be considered [107], while proponents of the two-interstitial model believe that static crowdions are also playing a role [108, 109].

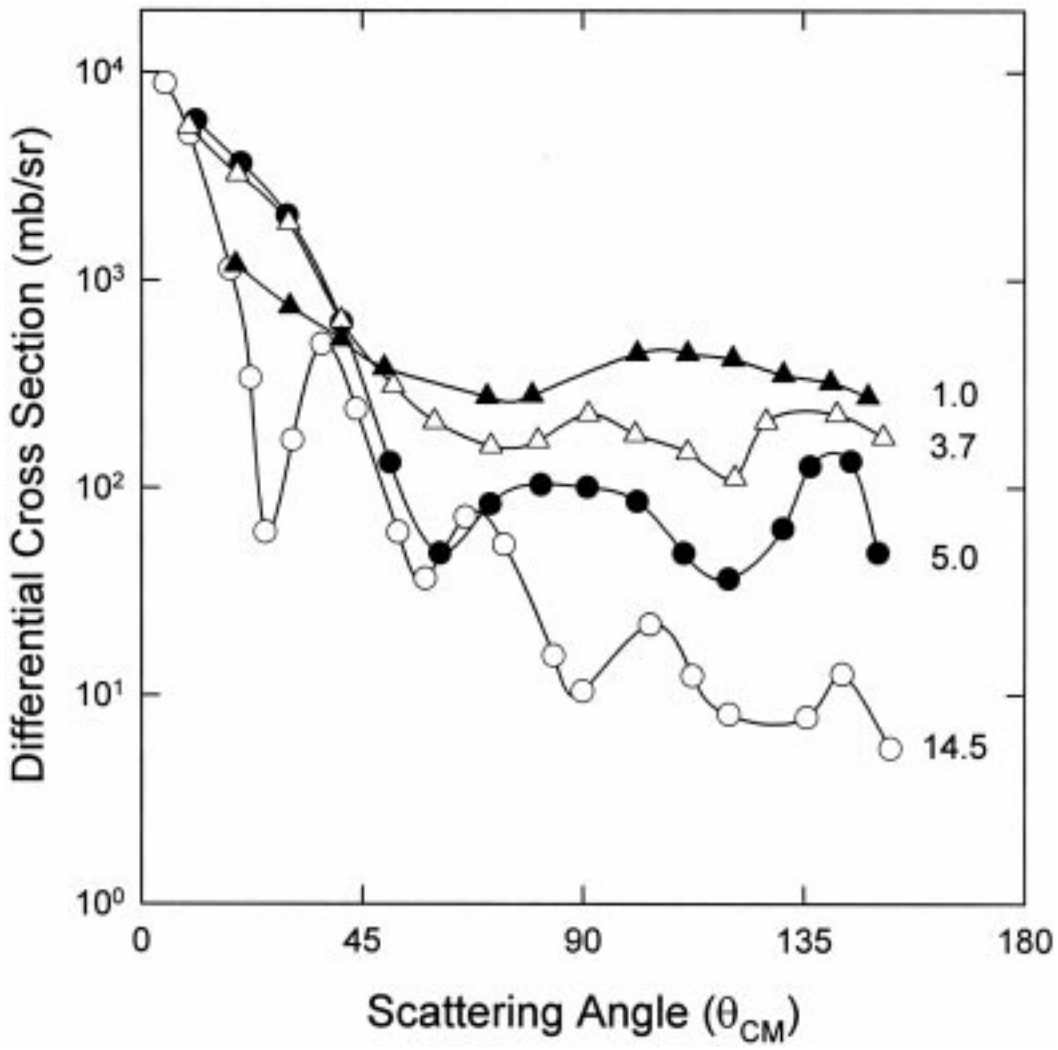

Figure 9: Differential cross sections for elastic neutron scattering on lead for energies of 1.0, 3.7, 5.0 and 14.5 MeV. The experimental data points are taken from references [103] and [104].

Stage I annealing occurs for most metals between approximately 15 and 60 K. Notable exception are iron and gold. In iron this stage appears at the relatively high temperature range of 100 to 120 K, while in gold Stage I annealing seems to be completed below 20 K despite relatively high defect retention. In Stage I, which is normally divided into 5 substages (Fig. 11), recombination of interstitial-vacancy pairs takes place. The first three Substages I_A, I_B and I_C are due to recombination of close Frenkel pairs with different crystallographic orientations, which recombine in a single step under influence of their mutual attractive stress field. The population of these three substages depends on the electron energy and their activation energies are typically of the order of 0.1 eV. Impurity and dose rate has little influence on close pair recovery. In some materials (Ag, Al and Ni) Substage I_A is missing.

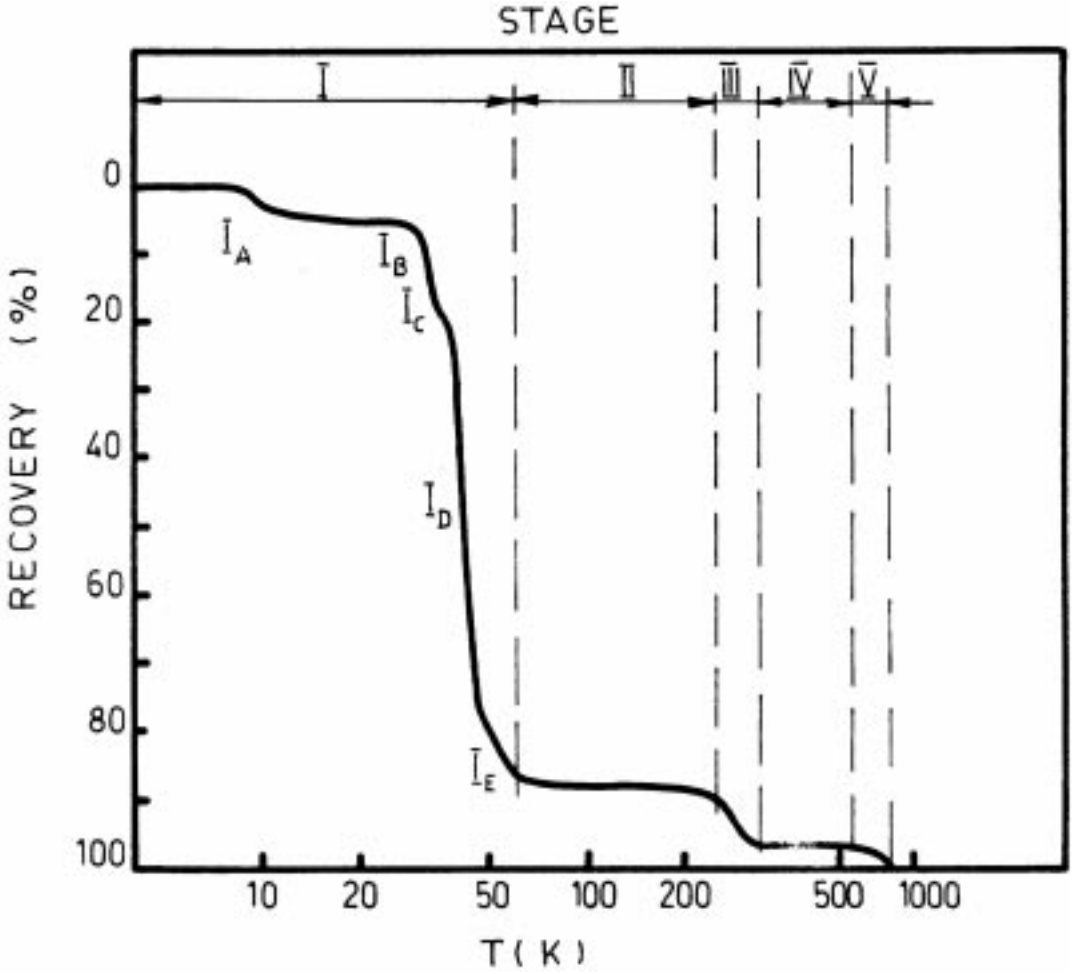

Figure 10: Isochronal recovery curve of electron irradiated copper. (From reference [105].)

The two higher Substages I_D and I_E are believed to be associated with recombination after free migration of interstitial atoms with their own vacancy (correlated recombination) and an unrelated vacancy (uncorrelated recombination) respectively. Free migration processes which result in uncorrelated recombination will, however, also lead to agglomeration of interstitials or trapping of interstitals at impurities and dislocations. It is expected that interstitials survive after Stage I mainly as di-interstitials or as interstitial-impurity complexes. The position and strength of Stage I_E is therefore depending on dose rate and impurity concentration. Stage I_E shifts to lower temperatures with increasing dose rate due to the higher defect density, which decreases the mean number of jumps necessary for annihilation with an unrelated vacancy. High impurity levels or dislocation concentrations lead to suppression of Stage I_E due to trapping of mobile interstitials. A similar effect occurs at very low damage concentrations, when all interstitials escaping correlated recombination will be trapped by impurities. Both effects lead to a higher retention of defects above Stage I, while quenched-in vacancies reduce defect retention.

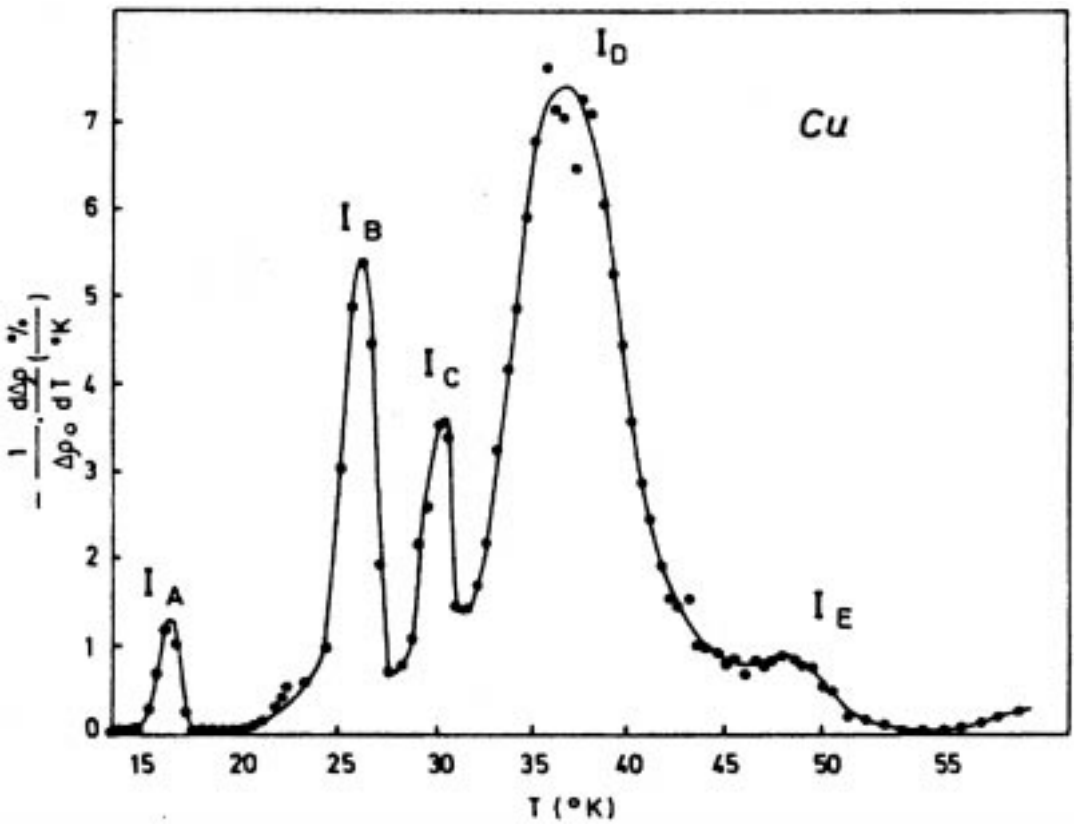

Figure 11: Stage I recovery spectrum of electron irradiated copper. (From reference [106].)

According to the two-interstitial model only metastable crowdions are involved in Stage I recovery, while the stable interstitials will only anneal at Stage III. This assumption implies that only crowdions are produced by electron irradiation, because otherwise the observed almost total defect suppression at irradiation temperatures above Stage I but below Stage III for prequenched samples cannot be understood. Thermal conversion to the stable interstitial, which is immobile below Stage III, is believed to be a result of crowdion-interstitial or crowdion-impurity interaction. Critics of this model argue that it should predict the disappearance of Substage I_E at low defect concentrations, as the restriction of crowdions to migrate only one-dimensionally (<110> in fcc) should force them to recombine with their own vacancies. However, initially defocussed replacement sequences might invalidate this argument.

A Stage III annealing peak at temperatures between 200K and 600K, which shows the characteristics of a freely migrating defect, has been generally observed in all metals. This peak shifts to lower temperatures with increasing dose. The one-interstitial model assumes that this is due to freely migrating vacancies which annihilate with trapped interstitials or interstitial clusters. This view is supported by the fact that activation energies extracted from these annealing peaks for pure aluminum, platinum and possibly gold agree with those obtained for vacancy migration in quenching experiments. Defect retention above Stage III is negligible in these three metals. For copper,

silver and nickel activation energies obtained for Stage III are lower than expected from quenching experiments, which might be explained as a strain field effect of interstitial complexes [110].

However, there are many experimental results which are difficult to explain within the one-interstitial model. One of the problems is presented by gold, where sub-stages I_D and I_E have never been found. In the frame-work of the one-interstitial model one has to make the somewhat unlikely assumption, that the reaction radius for interstitial-interstitial trapping in gold is large compared to interstitial-vacancy recombination. Alternatively it could be explained by the two-interstitial model by assuming that only the dumbbell configuration, which is immobile at Stage I, exists in gold. Furthermore, annealing of prequenched electron irradiated samples often show two Stages III and IV, which both exhibit characteristics of freely migrating defects and leading to activation energies for Stage IV in agreement with those expected for vacancy migration. Such stages were observed in *fcc* metals copper, silver, nickel and lead [111], where the activation energies for Stage IV agree with the activation enthalpies for vacancy migration as obtained from thermal-equilibrium measurements. A similar result was found for α-iron, where Stage III annealing is attributed to three-dimensional interstitial migration with enthalpy $H_I^M = 0.5$ eV, while Stage IV at 500 - 580 K is again assigned to vacancy migration with a $H_V^M = 1.28$ eV in agreement with thermal equilibrium measurements [112]. These results support the two-interstitial model, which assumes free migration of the stable dumbbell interstitial in Stage III and vacancy migration in Stage IV. Further support for this model comes from the study of the annealing behaviour of beryllium doped copper samples, which has been electron irradiated at temperatures just below Stage III [113]. The damage annealing during Stages III and IV for different irradiation doses is shown in Fig. 12. The increasing importance of Stage IV at the expense of Stage III at higher fluences is in agreement with the expected reduction of the concentration of interstial atoms due to an enhanced clustering probability. In a recent review article by Schüle [114] the existing experimental support for the two-interstitial model is summarized.

During electron irradiation only interstitials and vacancies are created, which are homogeneously distributed in space. The low energy transfer during an electron-atom interaction prevents the development of collision cascades and no defect clusters are therefore produced directly. Defect agglomeratation is a secondary process due to migration of point defects. In the case of interstitials, this process leads always to dislocation loops; while vacancies can also arrange themselves into voids or stacking fault tetrahedra [115]. During irradiation thermally activated point defect diffusion competes with radiation-induced diffusion. As far as the first process is concerned only interstitials are mobile at low temperatures. Their migration speed through the lattice is given by:

$$u = \nu d = \nu_0 d exp(-\frac{E_I^M}{kT}) \tag{20}$$

with *d* being the distance between adjacent interstitial sites. In pure metals this will lead to either

(a) annihilation with vacancies,

(b) creation of di-interstitials, which is the first step of loop nucleation,

(c) absorption by an existing interstitial loop, leading to its growth.

In doped metals a fourth possibility is the capture of a migrating interstitial by an impurity atom [116]. At the early stages of the irradiation (nucleation time) the processes (a) and (b) are dominating and an increase of the loop concentration is observed. At a later stage (growth time) the high vacancy and loop density is such an efficient sink for interstitials that process (b) becomes very unlikely and only processes (a) and (c) are important. Therefore, loop growth is then expected with the loop density reaching a saturation value. For the case restricted to interstitial agglomeration only, simple chemical reaction rate analysis can be employed to estimate the asymptotic loop concentration

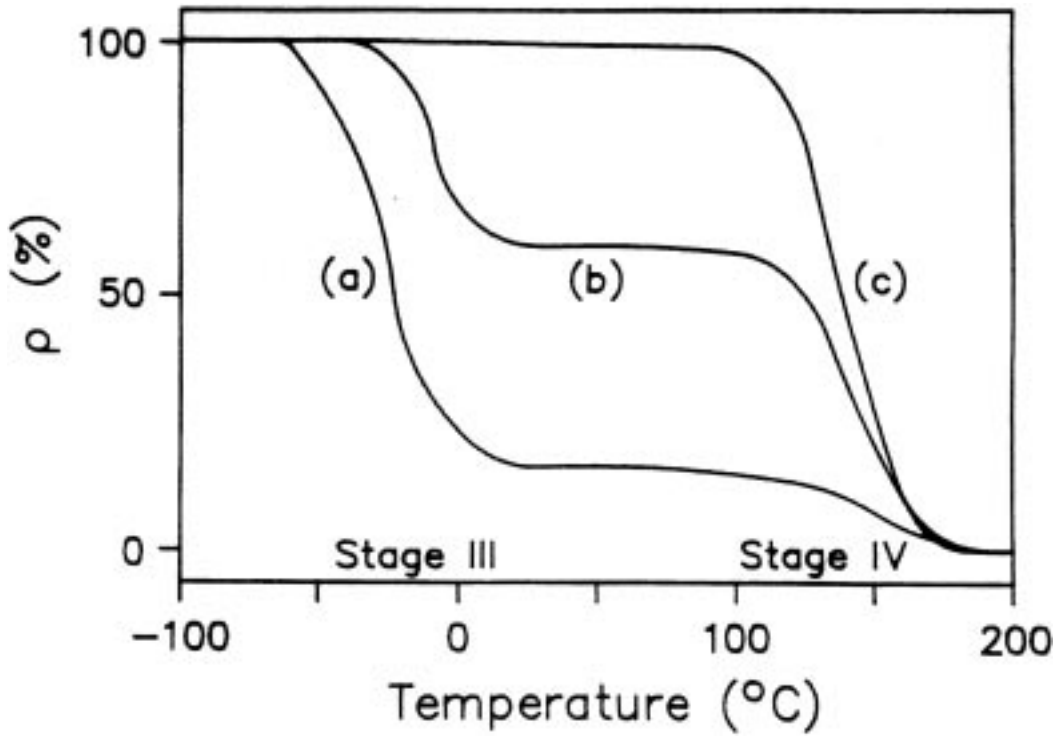

Figure 12: Stages III and IV recovery curves of beryllium doped copper for electron irradiation doses of (a) $\sim 10^{-6}$ dpa, (b) $\sim 3 \times 10^{-6}$ dpa and (c) $\sim 10^{-5}$ dpa. (From reference [113].)

[117, 12]

$$c^{\infty} = 0.7(\frac{G}{\nu_o})exp(\frac{E_I^M}{2kT}) \tag{21}$$

with G the interstitial generation rate per unit volume and time. If nucleation is impurity driven the final loop concentration is given by:

$$c^{\infty} = 2.6(\frac{c_K G}{\nu_o})exp(\frac{E_I^M + E_I^B}{2kT}) \tag{22}$$

with c_K the impurity concentration and E_I^B the binding energy of an interstitial by an impurity atom. At higher temperatures the situation becomes more complex as vacancies and defect clusters also become mobile, which will lead to a reduction of the final defect concentration. At high enough temperatures, which depend on the electron flux, no defect accumulation will occur. The above predictions are significantly modified if radiation-induced migration of point defects is also taken into account, as this allows the migration of both interstials and vacancies at low temperatures. This mechanism can be direct by transferring sufficient recoil energy to either an interstitial or an atom next to a vacancy, or indirect by creating a close Frenkel pair within the spontaneous recombination volume of an existing point defect, which then annihilates with his newly created anti-defect. One

consequence of radiation-induced migration is the development of vacancy clusters independent of the temperature, which eventually limits the growth of interstitial loops.

Experimental results, which were mostly obtained for thin foils in high energy electron microscopical studies, confirm these predictions if surface effects are properly taken into account [118, 119]. As the electron flux in a microscope is extremely high ($\phi \sim 10^{19}$ e $cm^{-2}s^{-1}$), nucleation time is normally much shorter than the observation time and results obtained are those pertaining to the growth time. In one of the first investigations [120] it was observed that dislocation loops are formed at room temperature in copper and aluminum, which grow in size with continued irradiation, while the loop density remains constant. Temperature dependent measurements [13, 121] show furthermore that loop densities decrease with increasing temperature and finally drop to zero.

Effects of irradiation-induced migration in lead were observed with high doses at temperatures below Stage III [122]. With increasing irradiation time the growth rate of interstitial loops was continuously decreasing until their average size reached a maximum — after which they started to shrink and eventually disappeared. Approximately at the time when interstitial loops reached their maximum size, vacancy clusters started to appear as stacking fault tetrahedra. The initial growth phase, during which only interstitial clusters appear, is due to the faster migration speed for interstitials than for vacancies, which only start to agglomerate after the density of interstitials has dropped sufficiently below that of vacancies. A state of equilibrium is then expected after which both cluster types should develop simultaneously. As the surface is a much more efficient sink for interstitials than for vacancies, shrinkage of interstitial loops is actually observed at high doses in high-voltage electron microscopical studies with thin foils. Because the migration energies are relatively low, irradiation-induced migration of interstials and vacancies in pre-damaged samples can also occur during bombardment with sub-threshold energy electrons, an effect which must be thoroughly taken into account during any electron microscopical investigation of radiation effects.

If metals are irradiated with high energy photons, similar defect structures are observed due to photo-electrons and Compton scattering. The latter produces recoil electrons with a maximum energy of:

$$E = \frac{2E_\gamma^2}{2E_\gamma + mc^2} \tag{23}$$

in the forward direction, which amounts to energies in the region of 1 MeV for a ^{60}Co source. The photo-effect is the dominant mechanism at low energies ($E_\gamma < 500$ keV) but becomes negligible compared to the Compton effect at higher energies. At much higher energies ($E_\gamma > 5$ MeV) electron-positron pair creation is dominating. However, the relative importance of the different mechanisms depends strongly on the atomic number of the target atoms [123].

B. Radiation Damage with Neutrons

Neutron irradiation can cause lattice defects by either nuclear reactions or scattering processes. Nuclear reactions are responsible for damage by thermal neutrons; while scattering is an important source of damage with fast neutrons. The resulting defect structures are vastly different; ranging from isolated Frenkel defects produced by radiative neutron capture, to large displacement cascades after high energy scattering events. However, displacement cascades can also be the result of energetic fission products, which furthermore, like most nuclear transmutations, introduce impurity atoms into the lattice.

Neutron capture reactions, which usually leave the compound nucleus in a highly excited state, have often very large cross sections at thermal energies. The de-excitation by high energy γ-radiation transfers a recoil energy

$$T = \frac{E_\gamma^2}{2M_r c^2} \tag{24}$$

to the atom with E_γ the energy of the emitted γ-ray and M_r the mass of the recoiling compound nucleus. Typically, this is of the order of a few hundred eV, which is sufficient to create a couple of Frenkel pairs. As typical γ-ray spectra of (n,γ) reactions are rather complex, recoil energies are usually spread over a considerable energy range. The average energy is nevertheless higher than obtained with electron beams, where low energy transfers dominate by far.

The recovery of (n,γ) damage after thermal neutron irradiation at low temperatures resembles to a large extent that obtained after electron bombardment [124]. However, additional close-pair recovery peaks below Substage I_D are observed [125], which might be due to the population of interstitial positions requiring higher displacement energies than those responsible for the well known Substages I_A, I_B and I_C. Furthermore, damage retention above Stage I_D is higher than observed after electron irradiation, while the magnitude of substages preceding I_D is significantly reduced. Both these features indicate larger average separations of Frenkel pairs due to higher mean recoil energies.

The energy spectrum of recoiling atoms after fast neutron irradiation ($E_n > 0.1$ MeV) is usually quite complex due to contributions of both elastic and inelastic scattering processes. The maximum energy which can be transferred is approximately given by:

$$T_{max} \sim \frac{4E_n}{M} \tag{25}$$

and displacement of lattice atoms can therefore be expected for neutron energies $E_n \gtrsim ME_d$. The mean recoil energy is much closer to the maximum transferable energy than in the case of charged particles, where the Coulomb interaction is strongly biased towards very small energy transfers. Consequently much higher recoil energies are transferred to lattice atoms by neutrons than by electrons.

Fast neutrons from nuclear fission have energies up to 15 MeV with a most probable value near 1 MeV. They produce mean PKA-energies in structural reactor materials in the region of 10 to 40 keV and large collision cascades are therefore expected. The defect density within an individual cascade will increase with increasing target mass. This is due to decreasing energy transfers and consequently larger scattering cross sections. Cascades in light targets are therefore quite large and diluted, while they are smaller and much more concentrated in heavy targets. Because of the high defect density in a collision cascade the survival rate of individual Frenkel pairs is low. Segregation of vacancies in the centre and the high density of interstitials at the periphery makes the escape of a point defect from a cascade rather unlikely. Most of them will either spontaneously annihilate or join existing clusters.

The higher defect density obtained during neutron irradiation compared to electron irradiation gives rise to radiation annealing, which manifests itself as a reduced damage production rate with increasing fluence. This is partly explained by the recombination of newly created defects with those produced previously [126], although other mechanisms like formation of defect clusters might also contribute. For room temperature irradiations of copper alloys with 14 MeV neutrons non-linear increases of defect densities were observed [127], which follow approximately a $\sqrt{\phi t}$ dependence

up to fluences of $\phi t \sim 10^{17}$ n cm^{-2}. As significant cascade overlap effects are only expected at fluences above 10^{18} n cm^{-2}, this is a clear indication that radiation-induced annealing occurs even if cascades are spatially separated.

The annealing of Stage I shows a broad distribution with only slight indications of the different substages. Most recovery takes place at the temperature of Substage I_D, while relatively little is observed in the region of close pair recovery. A major feature which distinguishes fast neutron damage from thermal neutron damage (Fig. 13) is the strong reduction of Substage I_E and a significantly higher damage retention above Stage I [125, 128]. Because of the segregation of vacancies

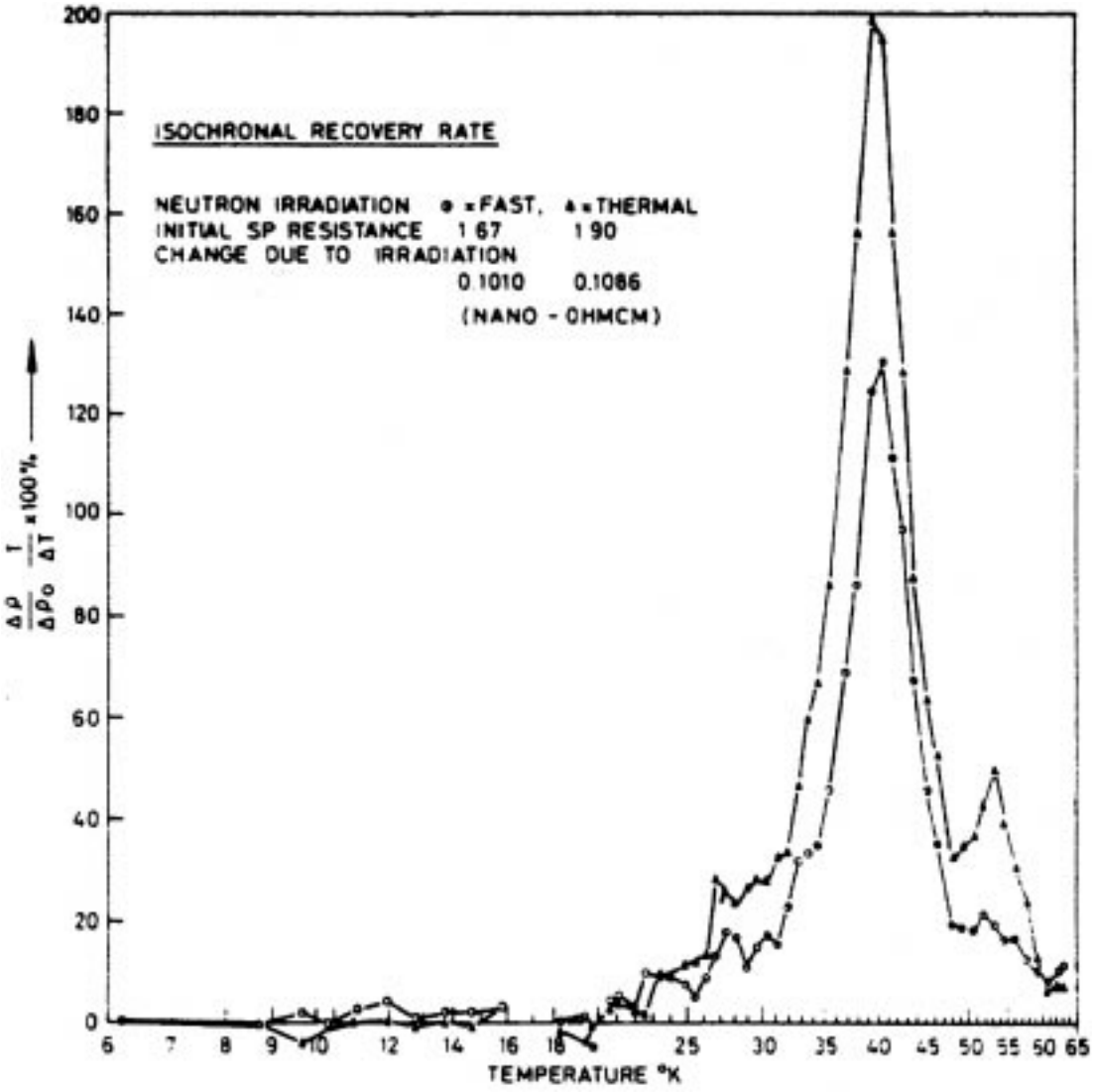

Figure 13: Comparison of Stage I recovery spectra in copper after fast and thermal neutron irradiation. (From reference [125].)

and interstitials, this general annealing behaviour of Stage I is expected. In such an environment the probability of an interstitial to interact with others to form stable clusters is quite high, while the existence of close pairs is rather unlikely. The suppression of Stage I_E is readily explained by the much higher probability of a single interstitial to annihilate with a vacancy belonging to its own cascade than to migrate to a different cascade, where vacancies are screened off by their own interstitials. As diffusion distances of interstitials to vacancies are short within a cascade, quasi-correlated recombination at Substage I_D is strongly enhanced. At higher doses cascades will start to overlap, but the argument in favour of Substage I_D annealing due to small diffusion distances still holds, although defect retention above Stage I will increase.

With fast neutrons a splitting of Stage III is observed. The higher component shifts to lower temperatures and eventually merges with the lower one at high doses. The activation energies of both components are similar and seem to agree with those for electron irradiations. The double peak is interpreted as quasi-correlated and uncorrelated annihilation of the migrating Stage III defect within and outside the dense damage zone of an individual cascade. Defect retention above Stage III is larger than for electron irradiation, but depends on the dose and mass of the target atoms. At an irradiation dose of 10^{19} n cm^{-2} at liquid helium temperature, defect recovery of about 70 to 80% above Stage III was observed in platinum, gold and silver, while complete recovery was obtained in aluminum. For the medium mass atoms nickel, copper and palladium recovery was in the range of 80 to 90% [129]. At irradiation temperatures above Stage III only defect clusters are observed, which in *fcc* metals consist of vacancy type stacking fault tetrahedra and triangular loops [127].

C. Radiation Damage with Light Ions

High energy protons, deuterons and α-particles can lead to similar recoil energies as with fast neutrons. However, due to the strongly decreasing elastic scattering cross section for small impact parameters, the probability for small energy transfers is dominating. The majority of recoiling atoms will therefore produce only a small number of Frenkel pairs and radiation annealing in pure and defect free metals is less pronounced than observed for fast neutrons. However, the introduction of point defect traps by either quenching, cold-working or alloying the samples prior to irradiation, leads to a significant increase of the initial defect production rate accompanied by strong radiation annealing effects [130]. In the case of proton irradiation, fast diffusion normally prevents any build-up of hydrogen in the target. However, hydrogen can be trapped by other impurity atoms leading to defect decoration [131, 132]. Surface craters have been observed after D_2^+ implantations in some metals [133, 134], which are attributed either to blisters created by deuterium coalescence or by clustering of point defects near the surface.

Damage retention after Stage I in light ion irradiated metals is significantly higher than found for electron irradiation [135]. The features of Stage I recovery is expected to be somewhere between those obtained with electrons and fast neutrons. This is illustrated in Fig. 14, showing a calorimetric Stage I annealing spectrum for deuteron-irradiated copper [136]. In the case of defect saturation, the close pair recombination peaks disappear for similar reasons as discussed for fast neutron irradiations. Furthermore, the Substages I_D and I_E merge together and shift to lower temperatures because the average distance between different Frenkel pairs approach the typical vacancy-interstitial distance of close pairs. Furthermore, defect retention increases because clustering of interstitials is becoming more probable. Cold-working and alloying will also increase defect retention during Stage I annealing [137].

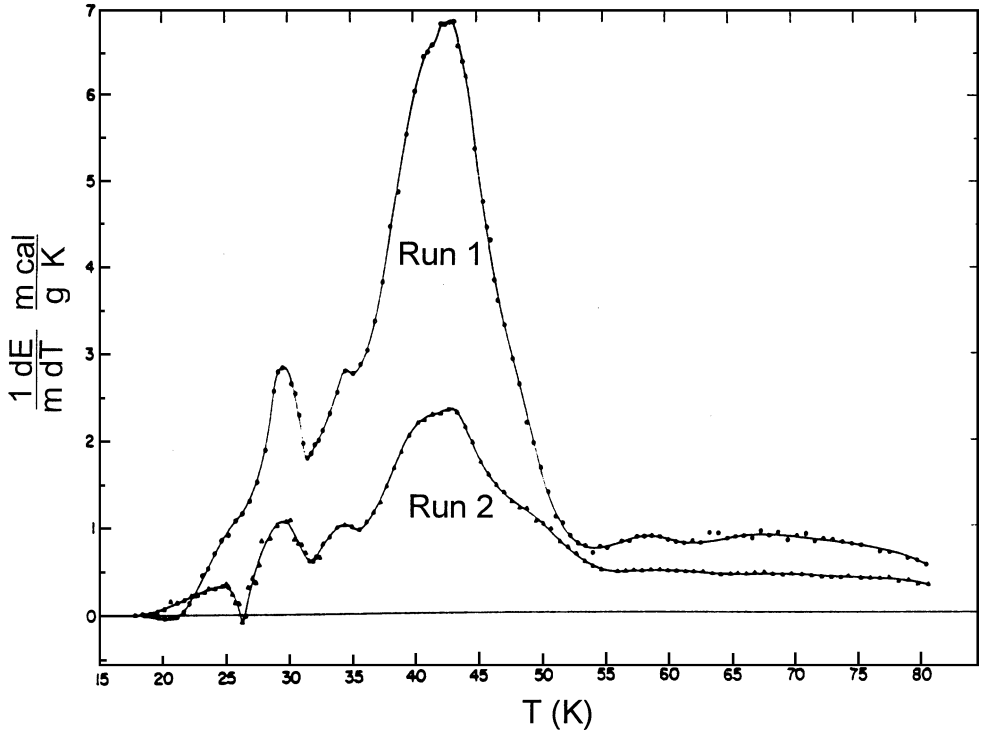

Figure 14: Calorimetric Stage I recovery spectra of deuteron irradiated copper for fluences of $\sim 8 \times 10^{15}$ cm^{-2} and $\sim 3 \times 10^{15}$ cm^{-2}. (From reference [136].)

Stage II recovery is mainly due to dissociation and rearrangement of impurity-interstitial complexes. Up to 3 substages are observed in some metals depending on the type of impurity. Intrinsic recovery in pure metals is small and is probably due to evaporation of interstials from larger agglomerates, which then recombine with vacancies. Few distinct peaks are observed; the features of the recovery curves depend sensitively on the defect structures present after Stage I annealing and are therefore depending on the initial irradiation conditions.

After Stage II recovery of pure metals the remaining defects are probably mainly di-interstitials and vacancies randomly distributed in the case of low initial defect density. However, as indications of more than one process in Stage III annealing is observed in some materials [138], an immobile interstitial configuration might also survive Stage II annealing. Therefore, what is normally grouped together as Stage III could possibly contain the two unresolved migration processes of dumbbell interstials and vacancies. In the case of slightly alloyed metals more stable impurity-interstitial complexes might also anneal during this stage, leaving only less stable complexes involved at Stage II recovery.

D. Radiation Damage with Heavy Ions at Medium Energies

Heavy ion implantation into metals will cause damage mainly by collision cascades, creating high vacancy concentrations in their core regions surrounded by less dense clouds of interstitials. The high

defect density of the depleted zones is conducive to further vacancy agglomeration, which can lead to the formation of voids and dislocation loops or stacking fault tetrahedra along closely packed lattice planes. Collision cascades near the surface may cause craters [139], which are often observed for low ion energy implantations [140]. At low fluence, overlap between cascade zones is unimportant and the damaged regions will form islands surrounded by a more or less defect free environment. However, with increasing fluence they will eventually overlap to form complex and very stable dislocation networks [141]. Creation of amorphous regions, which is often observed in non-metals is not expected in pure metals due to the non-directional property of the metallic bond. However, amorphization is observed in some alloys at low temperatures when defect densities become too high [142]. Not much microstructural change has been reported for irradiation temperatures $T \geq 0.6T_m$, but radiation induced segregation can occur in alloys at intermediate temperatures because of mobility differences of defects related to its constituent elements.

Direct investigations of damage structures have been conducted by employing transmission electron microscopy (TEM) and field ion microscopy (FIM). The latter technique has the ability of atomic resolution but allows only a very limited choice of target materials. A further limitation is given by the constraints of the target geometry, which effectively excludes investigations of defect configurations at positions where surface effects can be safely neglected. For determining damage profiles up to depths of the order of μm the indirect method of α-particle channeling in a backscattering geometry has been widely used.

Many spatial distributions of vacancies in an isolated collision cascade have been determined by FIM using a pulse field evaporation technique [143]. After low fluence irradiations of tungsten with energetic ions in the atomic mass range $40 \leq A_1 \leq 184$, relatively dense depleted zones were observed. Vacancy densities in these zones were found to be in the region of 10% to 20% for the heaviest ions and seem not to be strongly dependent on implantation temperature as long as this is kept below Stage III [144]. *In situ* observations of depleted zones produced by 30 keV ions at $T_i \leq 15K$ indicate a decreasing vacancy density with decreasing ion mass [145]. A significant result is the apparent stability of the depleted zones up to room temperature against collapse into lower energy configurations. This, however, seems to occur at room temperature with higher fluences, when cascade volumes start to overlap [146]. Non-linear effects due to cascade overlap were also observed for irradiation with heavy diatomic molecular ions . After break-up of the bombarding particle into two components, the near vicinity of their trajectories leads to an increased cascade overlap probability not only in space but also in time. Such events create large vacancy clusters embedded in a joint depleted zone. Fig. 15 shows a depleted zone in tungsten created by a single 40 keV Ag_2^+ dimer ion at $T \leq 10K$ containing a total of 675 vacancies, including two clusters of 329 and 110 vacancies each [147].

Apart from the collisional damage in the host lattice, impurity related defects are introduced except for the case of self-ion implantation. Their structures depend on a variety of parameters like solubility, diffusion coefficients and impurity-defect interactions. During the relaxation phase the impurity atoms can move into regular or interstitial lattice sites, be trapped by defects or diffuse out of the cascade region. Substitutionality of the implanted species is largely governed by the heats of solution [105]. For high fluences of non-soluble impurity ions segregation is often observed leading to precipitates [148, 149] or gas bubbles [150]. Phase changes can occur in alloys after high dose ion implantation [151].

A controversial aspect of radiation damage in metals by heavy ions is still the case of defects created far from the implanted region. From the energy distribution function of PKA's shown in Fig. 5

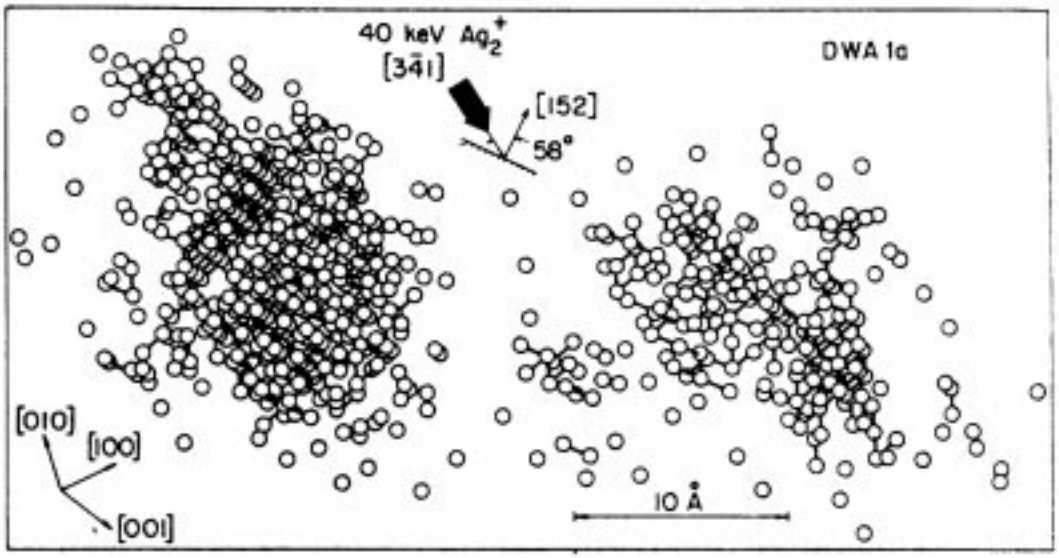

Figure 15: Depleted zone in tungsten created by a single 40 keV Ag_2^+ dimer ion at $T \leq 10K$. (From reference [147].)

it is evident that the total kinetic energy dissipated in a single cascade will on average be in the low keV range. Cascade diameters are therefore expected to be small compared to the ion range. Field ion microscopic analyses yielded typical diameters of less than 5 nm for depleted zones in tungsten [145]. The cascade size is therefore not expected to have a significant influence on the damage range. Monte Carlo calculations of depth distributions for primary defects display a maximum at a distance nearer to the surface than the projected ion range (Fig. 16). Experimental damage depth profiles were mainly determined by either electron microscopic or α-particle channeling techniques. In many metals, especially those with an *fcc* structure, much larger experimental damage ranges were found than expected from theory. Exceptionally large deviations from theoretical predictions were observed in copper [152, 153], platinum [154], silver and gold [155]. In one of the early studies [156] electron microscopy was used to investigate the depth distribution of vacancy and interstitial agglomerates in copper after implanting 5 keV argon ions. The distribution of the observed interstitial type dislocation loops (Fig. 17) extended to a depth at least five times larger than the projected range of approximately 4 nm for the argon ions. To explain this it was proposed that interstitials are moved deeper into the bulk by replacement collision sequences; after which they agglomerate to form interstitial clusters beyond the projected ion range. This would imply that interstitials are transported by focusons over distances of up to 40 lattice positions. Monte Carlo simulations, using for example, the code MARLOWE, confirm the occurrence of replacement collision sequences. But they rarely reach lengths of more than 10 lattice positions. It seems therefore rather unlikely that this mechanism is responsible for the observed enhanced damage range. This mechanism becomes even more unlikely if results obtained with higher implantation energies are considered. Taking the calculated energy distributions of PKA's into account, the above-mentioned mechanism should lead to damage ranges for argon ions in copper, exceeding projected ranges by a more or less constant value of about 15 nm, independent of the ion energy. However, experimentally determined damage ranges in copper

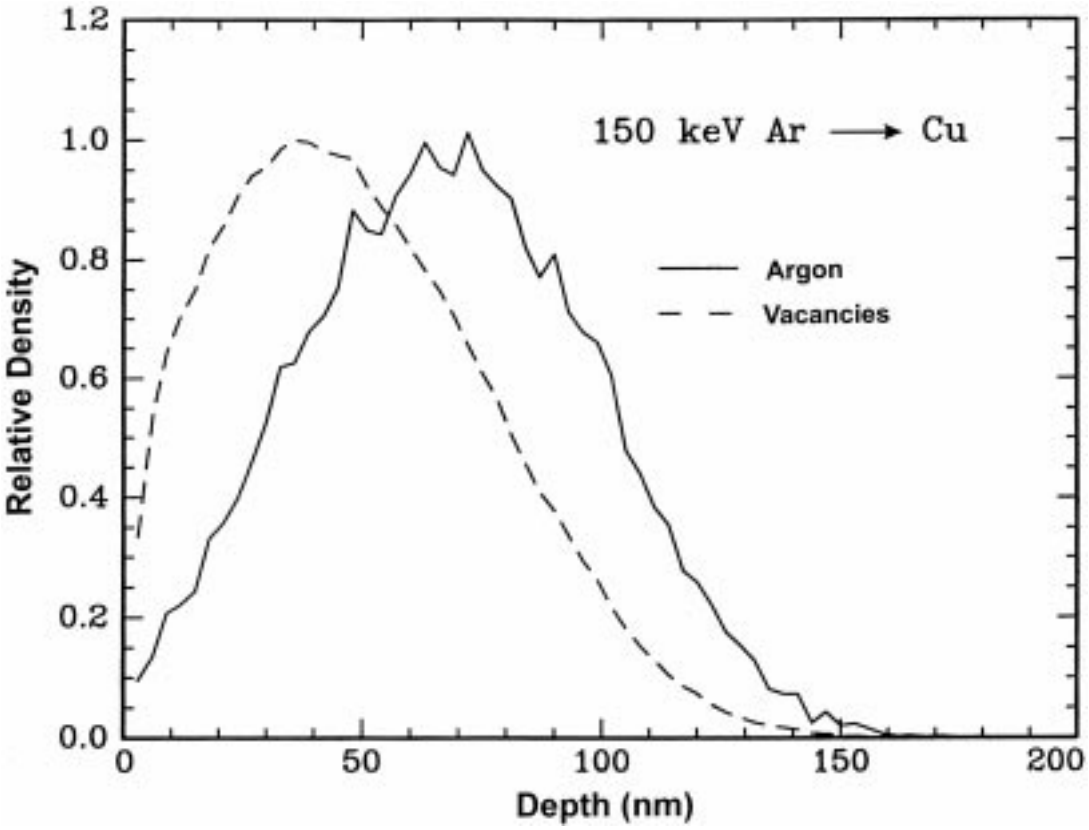

Figure 16: Predicted damage and implant distributions in copper for 150 keV argon ions according to TRIM simulations.

for a particular ion, determined by α-particle channeling in a backscattering geometry, are nearly linearly dependent on the ion energy [153, 157]. In the case of argon ions the thickness R_D of the damaged region extends approximately 5 times deeper than the projected range R_P (Fig. 18), which is similar to the factor found for the 5 keV implantation.

Interstitial transport by replacement collision sequences can therefore certainly not explain the extreme damage ranges found at higher energies. Because of the relatively high doses and the accompanying high damage levels, channeling effects can also not explain the observed large ranges [158]. As an alternative explanation it was proposed that deep damage is due to migration and eventual agglomeration of interstitials, which are thought to be copiously produced in collision cascades. However, according to molecular dynamic simulations discussed in chapter II-E, this last assumption is most probably not correct. According to such calculations, very few of the created interstitials survive the subsequent thermal spike phase. For a typical 5 keV cascade in copper only about a dozen interstitials escape recombination during this phase, which is significantly less than predicted by the modified Kinchin-Pease estimate.

More insight into the mechanism responsible for the enhanced damage ranges was obtained from systematic investigations of the effect different implantation parameters have on this phenomenon.

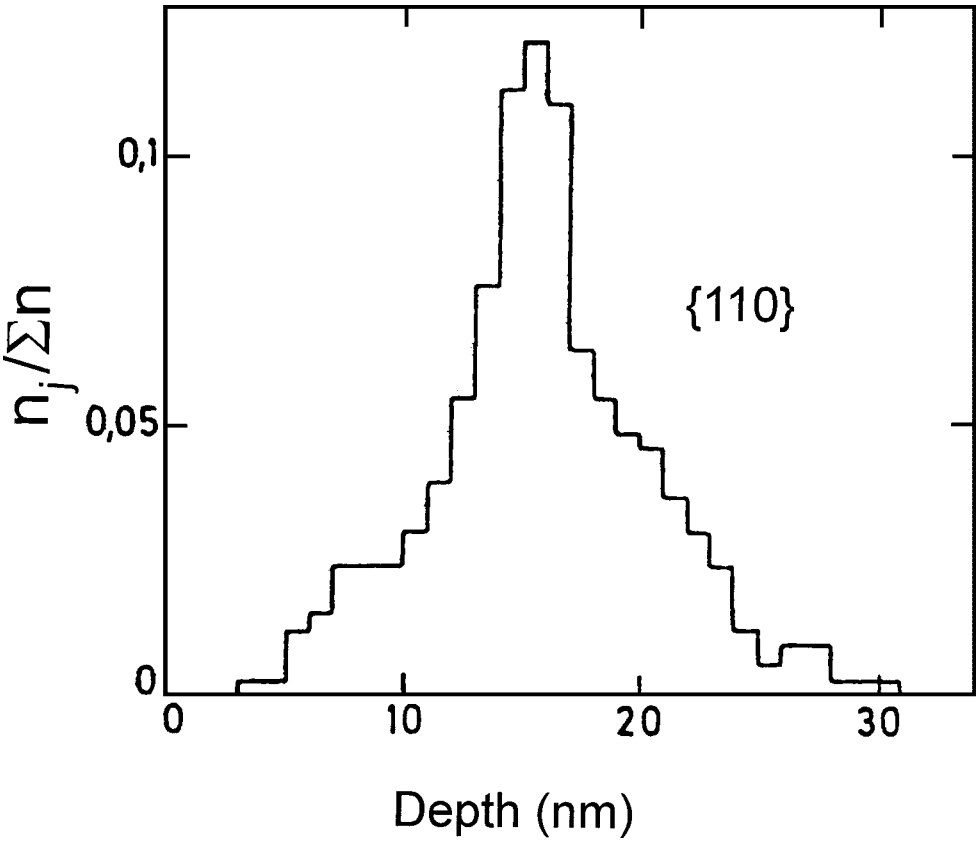

Figure 17: Depth distribution of interstitial dislocation loops in copper after implanting 5 keV argon ions. (From reference [156].)

An extensive study of a variety of ion-target combinations at different energies and temperatures [159] confirm the linear dependency of damage ranges on ion energy for a given ion-target combination (Fig. 19). For the investigated energies the relative damage range R_d/R_p is nearly independent of energy, but very different for different ion-target combinations. Obviously it increases for a given target with increasing ion mass as is illustrated in Fig. 20. For the heaviest ions damage ranges of almost 10 times the projected range were observed in copper. Some workers [160] report, that dense dislocation networks even occur 20 μm and 50 μm beyond the target surface after implanting 100 keV Ti^+ and Zr^+ ions respectively into copper with a fluences of 10^{17} cm^{-2}. This would imply defect formation in a region about 2000 times deeper than the projected range in the case of the heavier ion. It was suggested that this is due to the static and dynamic mechanical stress created in the implanted surface zone. No systematics of enhanced damage ranges concerning the target atomic mass is observed, but a dependence on lattice structure seems to be indicated as the largest deviations occur in metals with an *fcc* structure.

Most of the experimental results are difficult to reconcile with the mechanism of point defect migration, which assumes that mobile interstial atoms move deep into the bulk of the metal before they agglomerate to form stable dislocation loops. Especially the linear energy dependence seems to

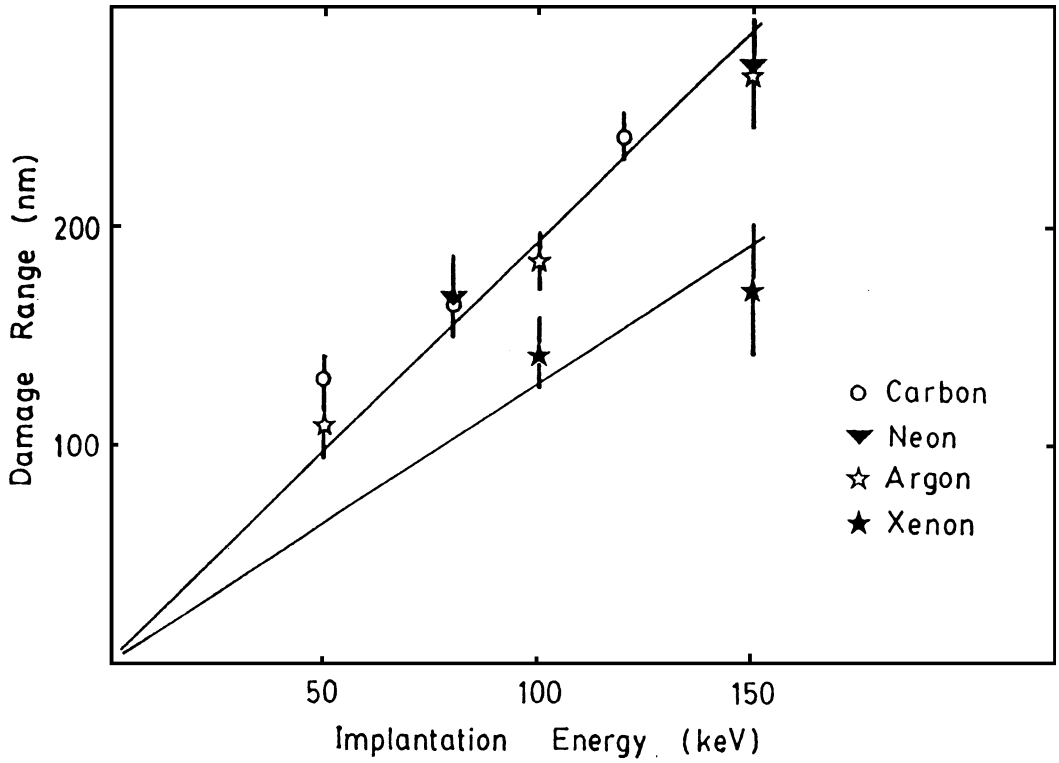

Figure 18: Experimental damage depths in copper for different ions as a function of ion energy. (From reference [153].)

be problematic, as it is not obvious at all why interstitial atoms created in a typical collision cascade should travel further in a lattice before being stopped simply because the implanted ion had originally a higher energy. It would also imply a dependence on activation energy, which should lead to similar damage ranges in all solids with comparable migration energies. In this respect it is noteworthy, that enhanced damage ranges are up to now only observed in metals and not in semiconductors and insulators, although their migration energies are comparable. Taking further the apparent structure dependence into consideration, a mechanism based on dislocation dynamics seems to be much more plausible.

According to the interstitial migration hypothesis, damage depth profiles should agree with theoretical predictions at sufficiently low temperatures, where point defect mobilities become negligible, while only a weak temperature dependence would be expected for a process driven by dislocation propagation. In order to distinguish between these two possible processes, implantations and *in-situ* analyses of copper and molybdenum single crystals were performed at low temperatures [155, 161]. Copper, which has an *fcc* structure, was chosen because of the large number of data already available for room temperature implantations, while molybdenum was of interest because of its different *bcc* structure. Implantations were done either below or just above annealing Stage I and defect profiles were obtained by α-particle channeling analyses. An experimental defect profile in copper after implanting 150 keV argon ions at 50 K is depicted in Fig. 21 together with the vacancy distribution

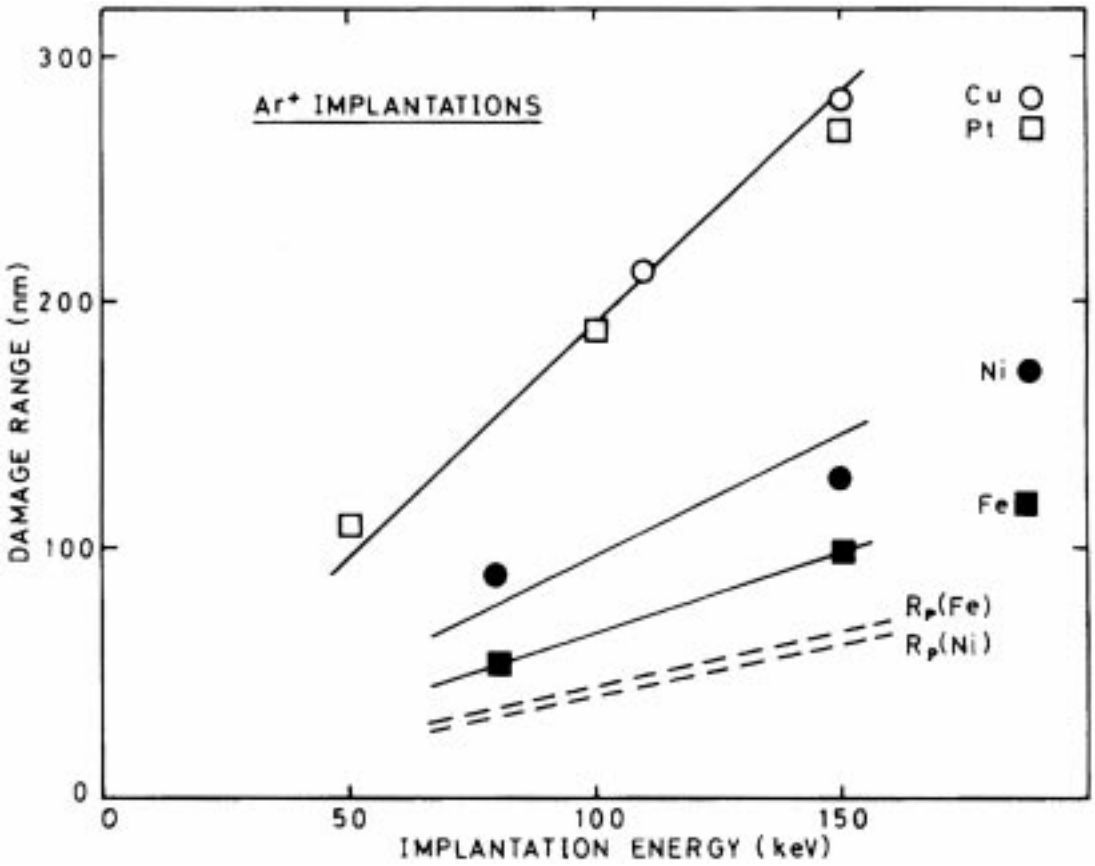

Figure 19: Damage ranges in some metal targets as a function of argon ion energy for room temperature implantations. (From reference [157].)

predicted by TRIM. The defect distribution, which disagrees radically with the theoretical prediction, did not change significantly during warming up to room temperature. The damage range, defined as the distance from the surface where the defect density drops to 50% of its maximum value, is approximately four times larger than the TRIM estimate of 85 nm. This is similar to the result found for room temperature implantations. A defect density profile for an implantation at 5 K is shown in Fig. 22. The damage range determined at this temperature is again about four times larger than the TRIM prediction. After warming up to liquid nitrogen temperature the defect distribution did not change within the experimental uncertainty. However, when the sample reached room temperature, a significant increase in the overall defect density was observed, although the damage range of approximately 330 nm was unchanged.

Defect profiles in molybdenum after argon implantation at 20 K are shown in Fig. 23 for various annealing stages. Also shown is the defect profile obtained after room temperature implantation, which is almost identical with the one obtained at the low temperature. After warming up from 20 K to 77 K practically no change is observed, but at the next two annealing steps at 182 K and room temperature appreciable increases of the defect density takes place. Similarly as with copper,

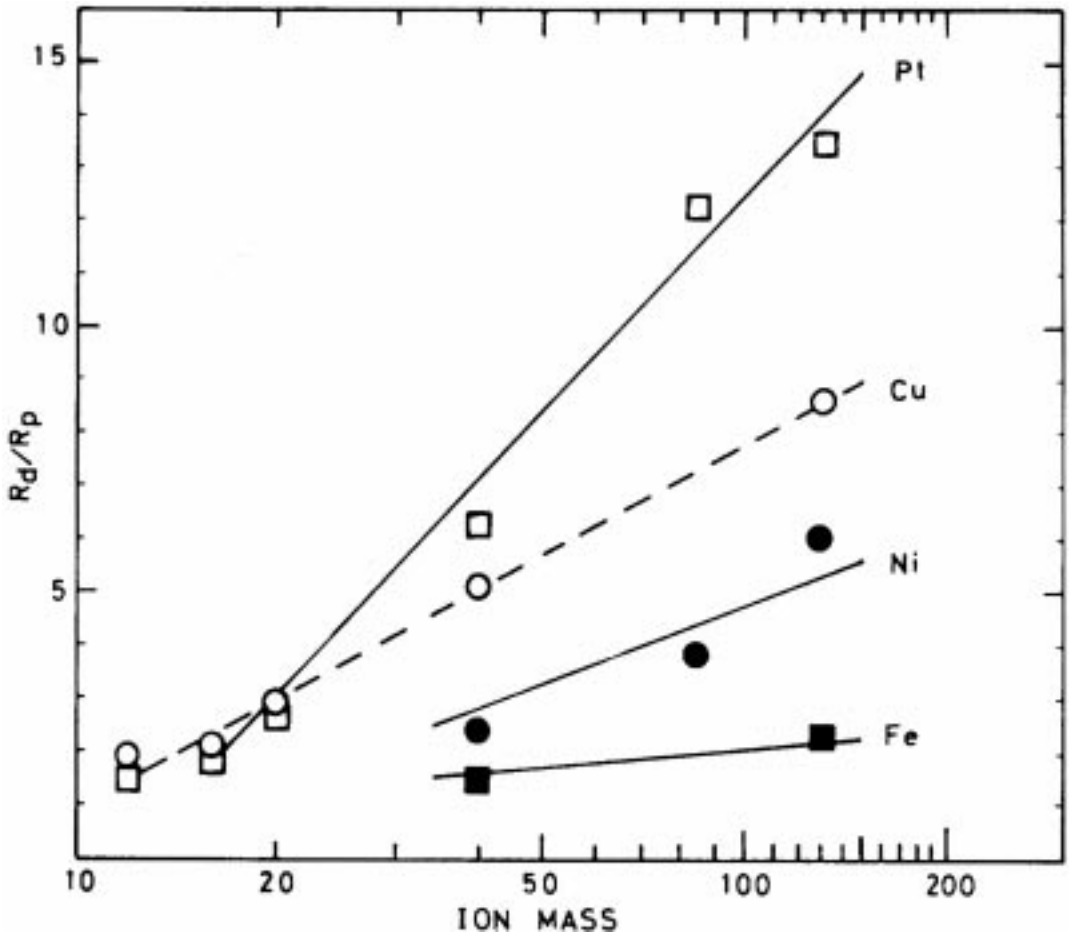

Figure 20: Relative damage ranges in some metal targets as a function of ion mass for room temperature implantations. (From reference [157].)

damage ranges are found to be independent of the implantation and annealing temperatures. Also, as is the case for copper, an increase of the relative defect density is observed for the cold implants only after warming up above liquid nitrogen temperature.

In both of the above-mentioned metals recovery Stage I is in the vicinity of 40 K. Only above this temperature free migration of interstial atoms is possible. The deviation of the experimental damage ranges from the theoretical predictions can therefore not be ascribed to long range migration of interstitial atoms. The stability of both defect profiles up to 77 K shows furthermore that mobile interstitials are not even available after passing recovery Stage I. Only at an appreciably higher annealing temperature the defect densities of the cold implants started to increase. This is possibly due to dissociation of interstitial clusters at recovery Stage II, which occurs somewhere between 100 K and 200 K.

The similarity of the defect profiles for implantations below Stage I and at room temperature implies, that even at room temperature, point defects do not have any significant influence on the defect

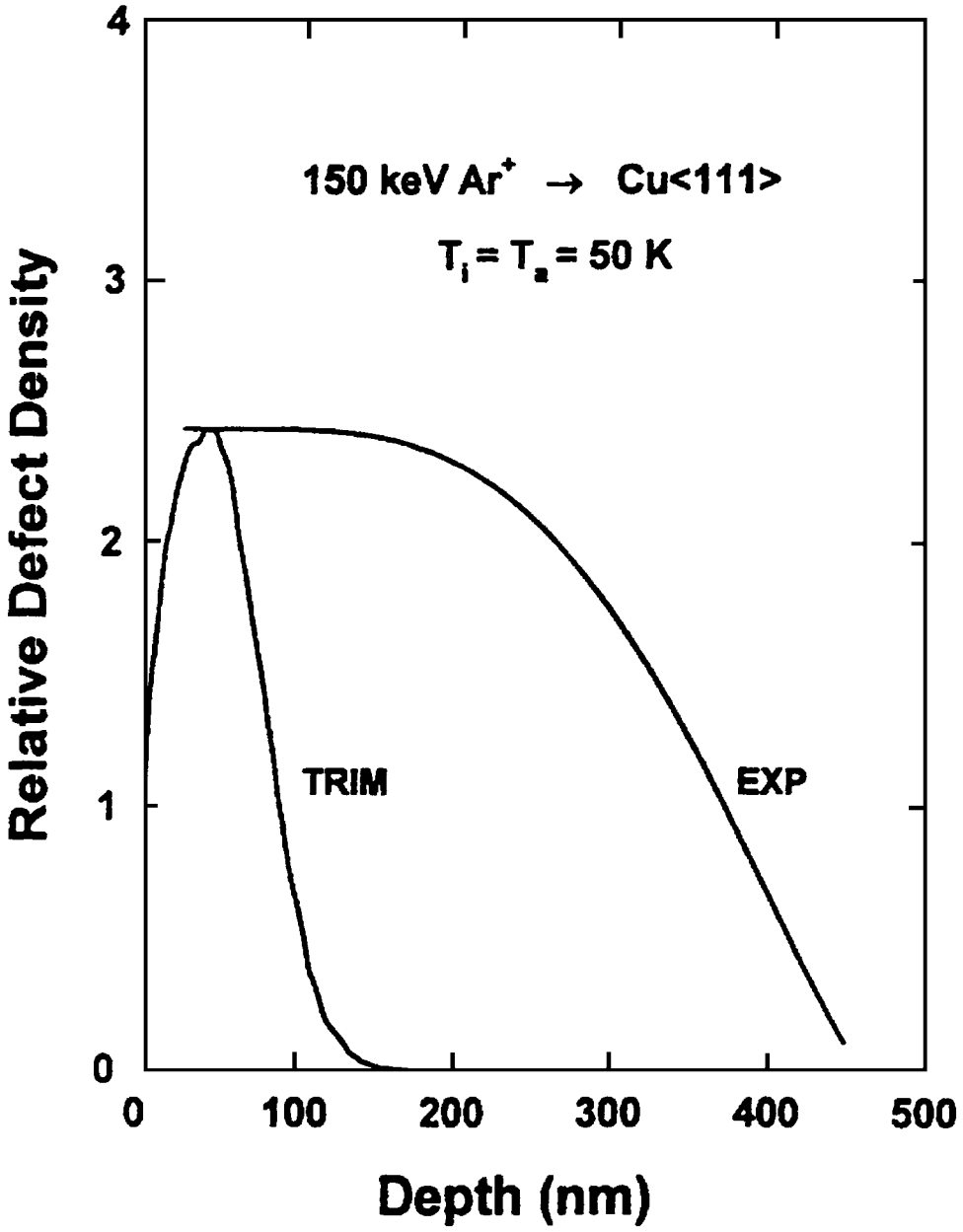

Figure 21: Relative damage depth profile in copper after implanting 5×10^{15} Ar^{+} cm^{-2} at 50 K compared with the vacancy distribution predicted by TRIM. (From reference [155].)

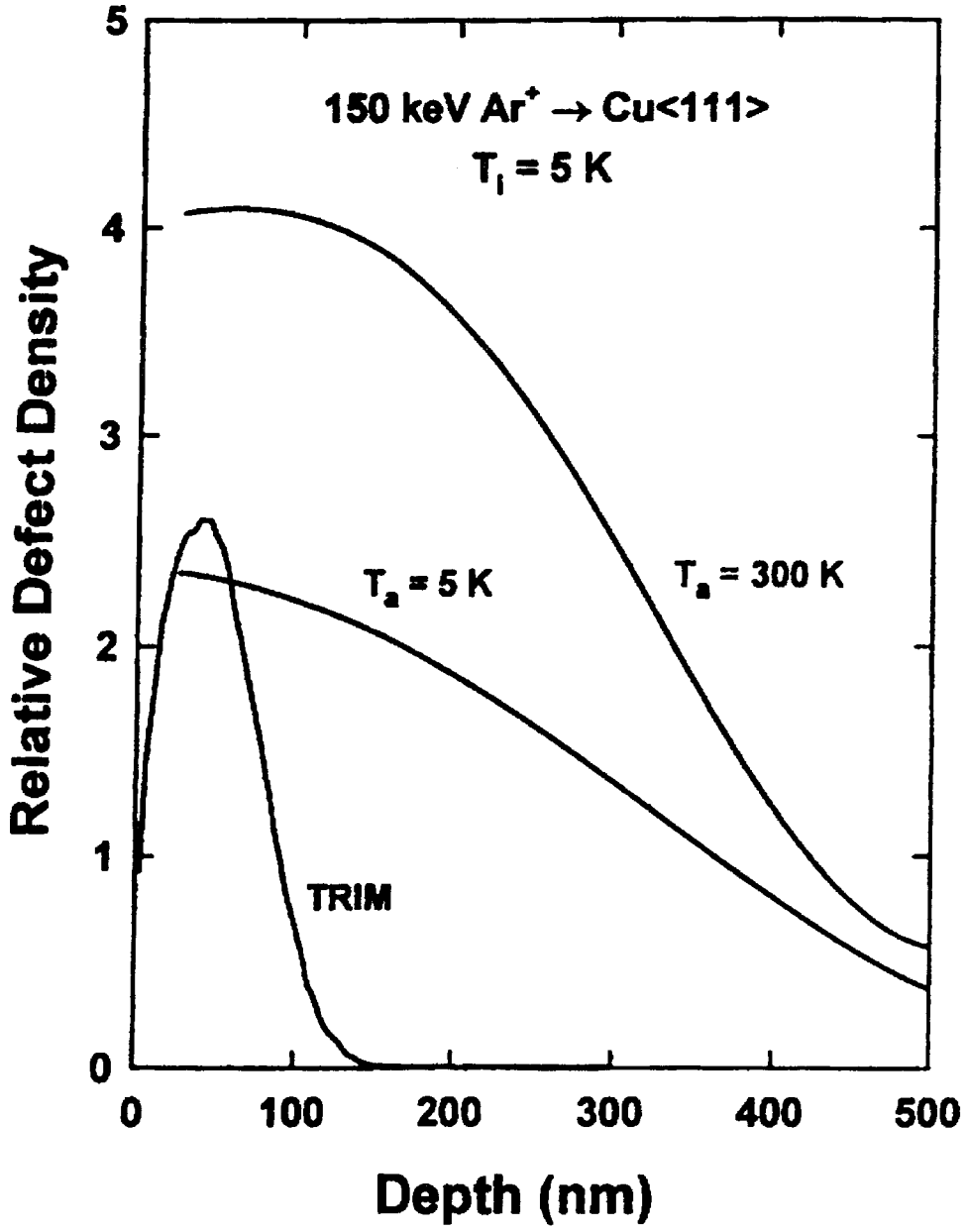

Figure 22: Relative damage depth profile in copper after implanting 5×10^{15} Ar^{+} cm^{-2} at 5 K and after warming up to room temperature compared with the vacancy distribution predicted by TRIM. (From reference [155].)

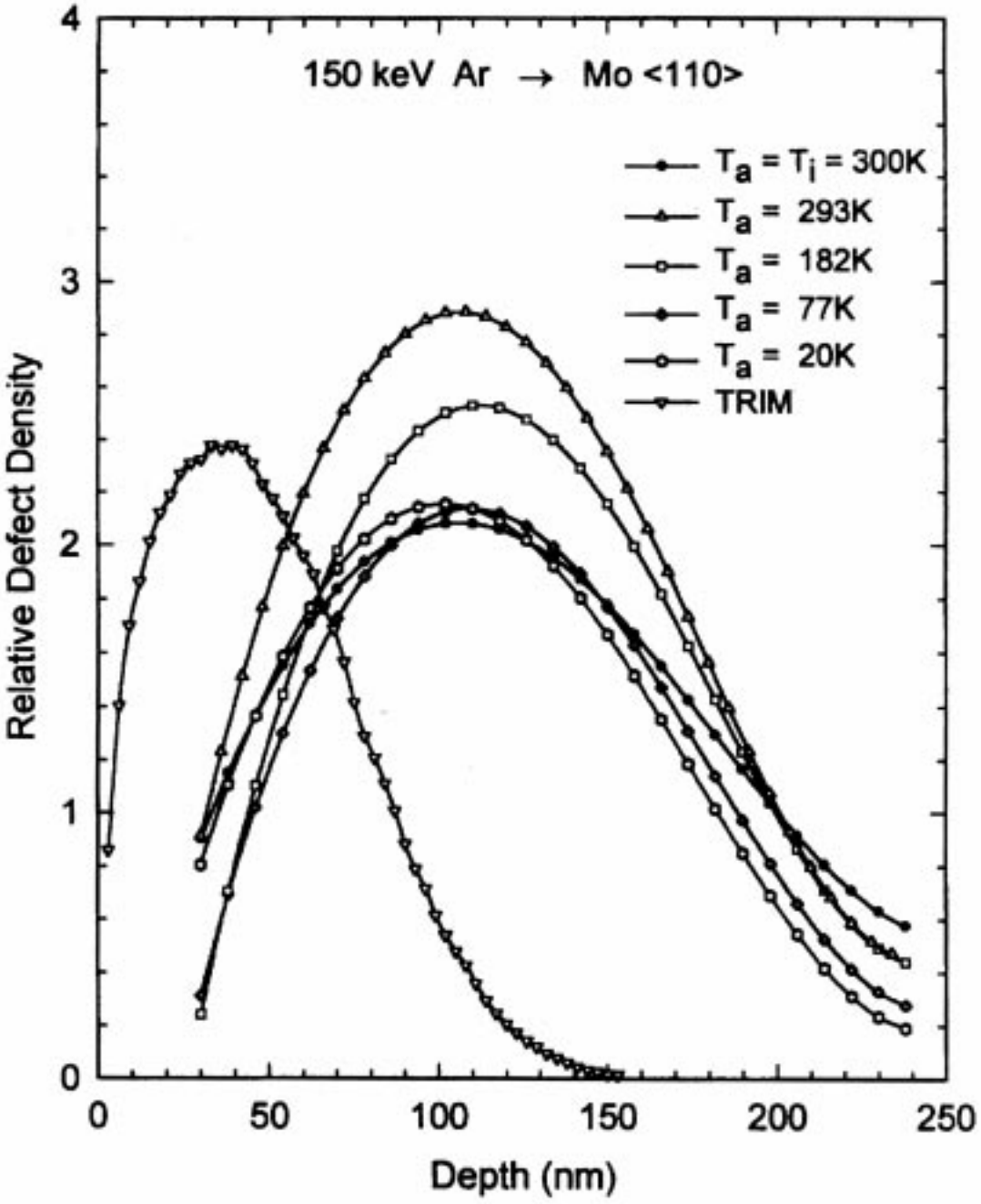

Figure 23: Relative damage depth profiles in molybdenum after implanting 5×10^{15} Ar^+ cm^{-2} at 20 K before and after warming up to 77 K, 182 K and 300 K. Also shown is the profile after room temperature implantation and the TRIM prediction. (From reference [161].)

density. This is probably partly due to the fact that only a small percentage of point defects created in collision cascades survive the subsequent thermal spike phase. As furthermore their mobility is high at room temperature, most of the remaining interstitials will escape from the implantation region without having any influence on the defect structure.

The situation is quite different for implantations below Stage I, where interstitial atoms cannot leave the implanted region. Therefore, with increasing point defect density in this region, interstitial atoms tend to form clusters which only dissociate at Stage II. After warming up above this temperature interstitial atoms are released from the clusters in relatively large numbers with mobilities still rather low and a much higher probability of being trapped in the now fully developed defect structure than in the previous case. This would explain the increases of the defect density at higher annealing temperatures observed in both metals after being implanted at temperatures below Stage I.

Table 1 summarizes the results for argon implantations into metals. From this table it is quite obvious that relative damage ranges in most metals are significantly larger than theoretically expected. It also indicates that this phenomenon is more pronounced in *fcc* than in *bcc* and *hcp* structures, although the difference is not very distinct and debatable in view of the limited number of investigated metals belonging to the last two groups.

Table 1: Relative damage depths after argon implantation in metals at different energies E_{Ar} and temperatures T_i analysed at temperature T_a. R_p is the theoretical projected range and R_d/R_t the ratio of the experimental and theoretical damage depth as defined in the text.

Material	Structure	E_{Ar} (keV)	T_i (K)	T_a (K)	R_p (nm)	R_d/R_t
Cu<111>	fcc	150	300	300	67	4.2
Cu<111>	fcc	150	50	50	67	4.2
Cu<111>	fcc	150	5	5	67	4.0
Ag<100>	fcc	150	300	300	69	3.9
Ag<100>	fcc	130	77	300	60	4.4
Au<311>	fcc	130	77	300	47	5.3
Pt<111>	fcc	150	300	300	48	4.3
Pt<111>	fcc	150	77	300	48	4.8
Pd<111>	fcc	150	300	300	57	2.9
Pd<111>	fcc	150	77	300	57	3.3
Ni<100>	fcc	150	300	300	63	2.4
Fe<111>	bcc	150	300	300	67	1.5
Mo<110>	bcc	150	300	300	67	2.3
Mo<110>	bcc	150	20	20	67	2.3
Co<0001>	hcp	150	300	300	64	1.7
Re<0001>	hcp	720	300	300	220	1.1

To understand the deviations from the theoretical damage profile depicted in Fig. 16, one has to bear in mind that the vacancy distribution computed by TRIM does not account for dynamical processes taking place after the initial collisional phase has subsided. Especially the sharp density fluctuations [162] expected during the thermal spike phase (Fig. 24) can profoundly impact on

the final defect structure. As the time in which an individual ion is stopped is much shorter than the life time of the thermal spike phase, all collision cascades along a particular ion track interact simultaneously with the crystal lattice. This should give rise to a shock wave, which could dissipate its energy by a variety of interactions with the lattice. Some of them can lead to the creation of dislocations. The depth beyond the ion range at which dislocations can still be produced depends on the rate at which the energy is transferred to the lattice and on the minimum energy needed to create a dislocation. Because of this latter factor, the observed damage depths should somehow reflect the structure dependence of the Peierls force. This force, which is the minimum force needed to move a dislocation in a lattice, is known to be small for *fcc* lattices and furthermore depends only weakly on temperature. The results listed in Table 1 seem to support an explanation of the observed enhanced damage ranges in metals by such a mechanism.

E. Radiation Damage with Heavy Ions at High Energies

For heavy ions with energies in the region of several MeV per nucleon, stopping is mainly due to inelastic electronic excitations while the cross section for elastic encounters with the target atoms becomes very small. Until about a decade ago it was therefore believed that swift heavy ions would not cause any damage in metallic targets. The general consensus was that the rapid smearing out of perturbations in a free electron gas would prevent localized energy transfer to the crystal lattice. According to this argument the energy deposited near an ion track is distributed in a very short time ($t \lesssim 10^{-14}$ s) over a large volume while the high mobility of Bloch electrons would almost immediately screen off ionized atoms. This would effectively prevent local melting and Coulomb repulsion effects. Of course such an argument is only valid as long as the magnitude of the perturbation does not exceed a critical value above which sufficient energy is transferred to the lattice during the electronic relaxation time to cause damage. This critical energy deposition density will depend on the electronic and thermal properties of the target material.

The first evidence of amorphization of a crystalline metallic alloy by electronic stopping of 3 GeV uranium ions was published in 1990 [163], while structural changes in metallic glasses had already been observed some years before [164, 165]. With the growing availability of heavy ion beams in the GeV energy range a large number of further cases including alloys [166, 167] and pure metals [167, 168, 169, 170] were reported in the following years. The threshold for damage by electronic interaction is found to be in the stopping power region of $|dE/dx|_e \gtrsim 10$ keV/nm. Metals sensitive to electronic slowing down of fast heavy ions include bismuth, gallium, titanium, cobalt, zirconium and iron. In addition to this inelastic damage production, annealing of defects created by elastic collisions were detected in iron, nickel, niobium and platinum [171, 172]. On the other hand, no sensitivity to electronic stopping has yet been observed in metals like copper, palladium, tin, tungsten and gold. Of course this separation in two groups is somewhat artificial, as it is obviously based on the current limitations of available experimental stopping powers. By extending experiments to still higher stopping powers, as are for example attainable with high energy heavy ion clusters, the last group of metals might also display electronic stopping effects.

Because of the relatively low fluxes of fast heavy ions generally available, damage is mostly observed as isolated latent tracks due to single ions. Normally they consist of amorphous or disordered zones in alloys [173] and highly defective crystalline structures in metals, including transformation to high-pressure phases [174]. For electronic stopping powers near threshold, tracks often consist of a row of droplets, while continuous cylindrical strings of damaged material is observed with higher stopping powers [169, 175, 176]. Track radii are of the order of 10 to 30 nm and are for a given

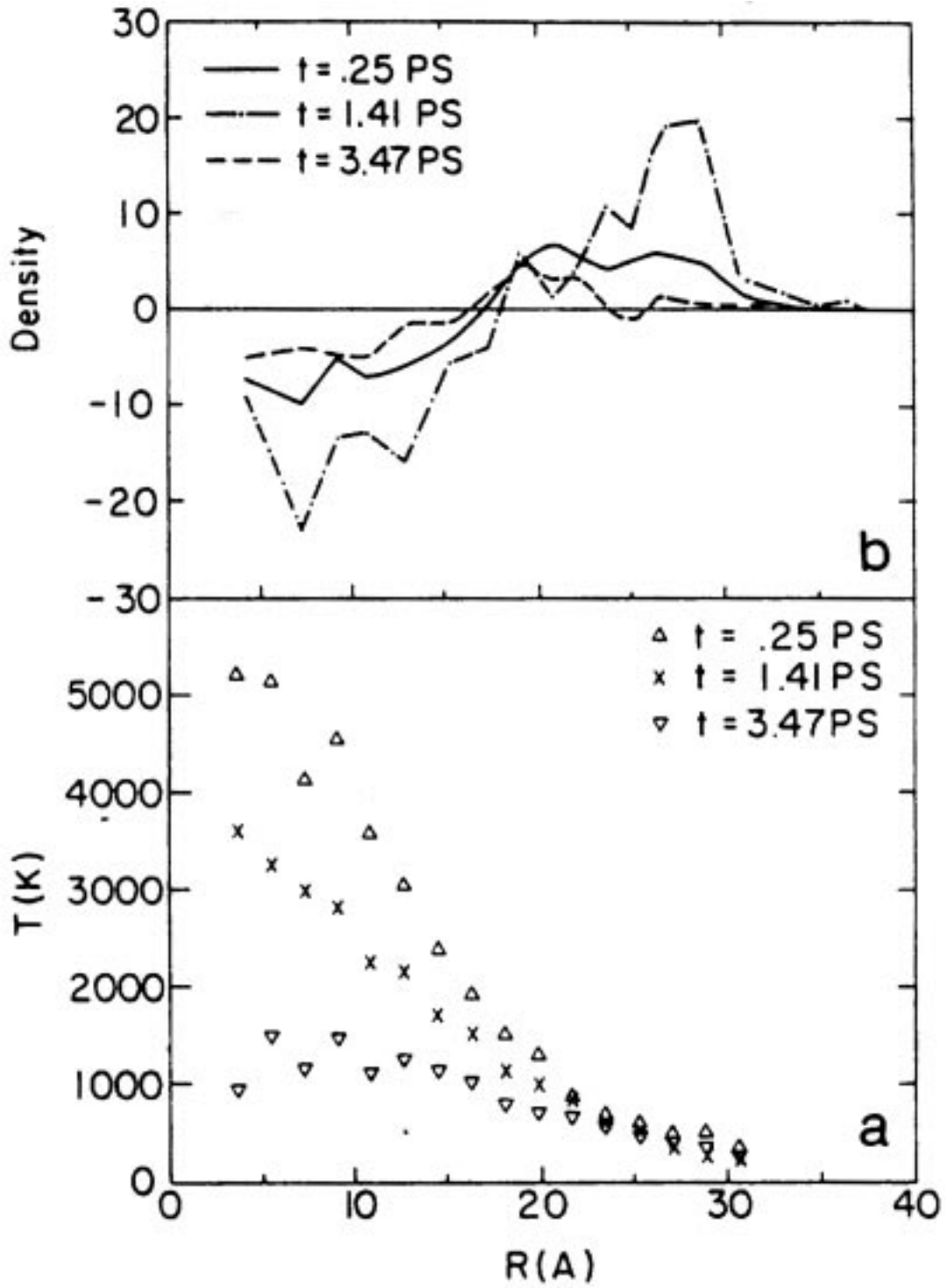

Figure 24: Density and temperature profiles for a 5 keV cascade in copper at three instants of time. (From reference [162].)

stopping power inversely dependent on ion velocity [177]. Annealing experiments of low temperature irradiated samples show a complete absence of Stage I [170], proving that no Frenkel pairs are present. Plastic flow of material perpendicular to the ion trajectory occurs in amorphous targets above an incubation fluence [178, 179, 180, 181, 182, 183, 184]. This anisotropic deformation exhibits no saturation at high fluences and leads to target shrinkage along the beam direction without volume change. This seems to be a universal phenomenon in all amorphous solids but does not occur in crystalline materials. In this context it must also be noted that the sensitivity to electronic stopping is much higher in an amorphous alloy than in its crystalline counterpart [185].

Two different theoretical approaches have been employed to explain defect production in metals by electronic stopping:

1. Thermal Spike Model. [186, 187, 188, 189, 190, 191, 192, 193].
2. Coulomb Explosion Model. [167, 178, 194, 195, 196, 197]

The Thermal Spike Model assumes that sufficient energy is transferred from the electron gas to the lattice to melt the immediate neighbourhood of the ion track, which then recrystallizes during rapid quenching. This can be considered in a first approximation as a mechanism consisting of three independent steps. In the first step the electron gas is heated by δ-electrons having typical flight times of the order of 10^{-15} s. Energy transfer to the lattice during the second step is then governed by the electron-phonon coupling constant g_{ep} and is equal to $g_{ep}(T_e - T_l)$ per unit volume and unit time, with T_e and T_l the instantaneous temperatures of the electron gas and lattice respectively. The coupling constant depends on Debye temperature, electron density and electronic thermal conductivity. Parameters governing the final step of melting and recrystallization are specific heat, melting temperature, latent heat of fusion and lattice thermal conductivity. According to this model materials sensitive to electronic stopping should be those with strong e-p coupling and low melting temperatures. Comparison of experimental results with theoretical predictions concerning track radii and electronic stopping power thresholds show fair qualitative agreement. The much higher sensitivity of amorphous metals can also be understood in terms of the significantly lower electron mobilities than in the crystalline state. Furthermore the annealing effect of electronic stopping, which manifests itself as a decreasing damage efficiency of nuclear stopping, can be satisfactorily described by the Thermal Spike Model [192, 193].

An alternative explanation for the electronic stopping sensitivity of metallic solids makes use of the Coulomb Explosion Concept, which already has been successfully applied to insulators. In this view an highly ionized cylindrical region is created along the ion track with a lifetime long enough to displace atoms by the repulsive Coulomb forces. The primary ionization by inelastic collisions of swift heavy ions produces a relatively high density of δ-electrons, which causes secondary ionization in a shell around the original ion track. The total space charge along the ion track is expected to build up in a time much shorter than one plasmon period ($\sim 10^{-16}$ s) and should not survive longer than 10^{-15} s in metallic systems before being screened off by conduction electrons. During this time a radial impulse acts on atoms within the ionized region transferring an energy of the order of 1 eV/at. This is sufficient to overcome energy barriers between regions of different atomic configurations in metallic glasses, which would explain the observed anisotropic plastic deformation in amorphous targets. In a crystalline target displacement energies are approximately one order of magnitude

larger and only phonons can therefore be excited. Such a collective excitation can produce strong dynamical disorder in materials with low frequency phonon modes, which may lead to displacive phase transitions in metals or amorphization in alloys. Strong evidence for this mechanism is the observed dependence of the damage cross section on electronic stopping power in titanium and iron as illustrated in Fig. 25. In this representation the damage cross section is plotted as a function of the

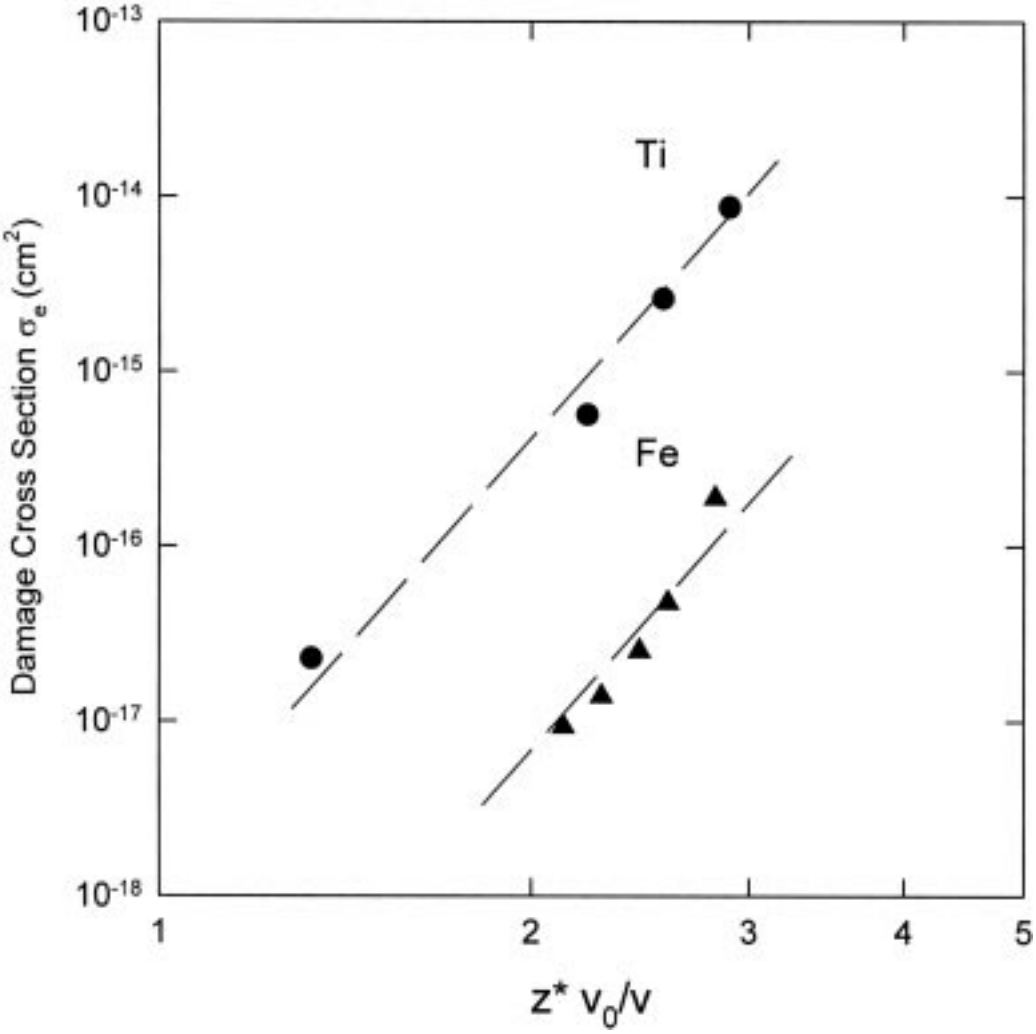

Figure 25: Cross section for damage creation by electronic excitation in Ti and Fe as a function of $\eta = z^* v_0/v$. The doted line corresponds to an η^8 relationship. (From reference [196].)

dimensionless parameter $\eta = z^* v_0/v$ with $z^* e$ the ion's effective charge and η^2 roughly proportional to the electronic stopping power. The experimental results [171] indicate a $|dE/dx|_e^4$ relationship in agreement with theoretical expectations [196].

F. Spatial Ordering of Irradiation Induced Defect Structures

An intriguing phenomenon is the often observed ordering of defect structures after high-dose particle irradiation of metals and alloys, displaying a regular pattern related to the lattice structure of the material. Such self-organized structures have been observed for extended defects like voids [198, 199, 200], gas bubbles [201, 202], stacking-fault tetrahedra and planar defect walls [203, 204]. Ordering of voids evolves from a uniform defect distribution during implantation of heavy ions or fast neutrons at high-temperatures ($T_i \sim 0.3\ T_m$). In *fcc* and *bcc* metals they display a three-dimensional lattice structure similar to that of the host material, while in *hcp* systems only two-dimensional ordering takes place leading to hexagonal void layers parallel to the basal plane. The ratio of the lattice parameters of the defect and crystal structure depends on the material and is not much influenced by irradiation conditions. Bubble lattices form at ambient temperatures and conditions resembling those for void lattices during implantation of inert gas ions. However, their lattice parameter ratios and bubble radii are smaller than those found for void lattices. Characteristic properties of such superlattices are uniform defect sizes and high stability against thermal and irradiation annealing. The evolution of superlattices starts at low fluences with the growth of randomly distributed defect structures, which gradually align themselves with increasing fluence along crystallographic directions of the host lattice. This alignment starts at first in some isolated regions, which eventually grow together, typically exhibiting edge dislocations at their boundaries. Other imperfections like vacant sites do also normally occur. Fig. 26 [199] shows a typical ordering of voids in molybdenum after implanting 2 MeV nitrogen ions with a dose of approximately 10^{18} cm^{-2} at 870 ^0C. The voids display a *bcc* structure with a superlattice parameter of ~ 22 nm and axes in exact coincidence with the crystallographic orientations of the underlying molybdenum lattice. Self-organization of stacking-fault tetrahedra occurs during irradiation with 1 MeV electrons and fluences above 10^{23} e$^-$ cm^{-2} in copper and silver at temperatures of 150 K $\lesssim T_i \lesssim$ 350 K [203]. At the lower end of this temperature range simple cubic patterns are observed with a lattice parameter of approximately 7 nm, while at the higher temperatures periodic defect walls appear. Planar walls of point defect agglomerates with a periodicity of 60 nm have also been obtained in copper during high-dose irradiation with 3 MeV protons [204].

A number of theories have been put forward to explain the occurrence of self-organized microstructures induced by high-dose irradiations. Although different mechanisms occurring at largely different irradiation conditions are probably responsible for the ordering of different defect types, the general reason is anisotropic and energy-dissipative matter transport under non-equilibrium conditions. One process belonging to this kind is point defect clustering during random Frenkel-pair production [205, 206], which is assumed to form the basis of the observed ordering of stacking-fault tetrahedra after prolonged electron irradiation [207]. An analysis applying rate theory to model the evolution of immobile point defect clusters interacting with mobile point defects [208] was able to show that a uniform distribution of defect structures becomes unstable at high doses, leading to the formation of regular patterns with a transition to defect walls at still higher fluences. This mechanism, however, cannot explain the formation of void lattices at elevated temperatures, where the highly mobile interstitials prevent a built up of the necessary monovacancy concentration. An alternative explanation for void lattices has been proposed in terms of the two-interstial model [209, 210]. According to this approach the difference in dynamical anisotropy of crowdions, which can only move one-dimensionally, and dumbbell interstitials, moving three-dimensionally through the lattice, causes neighbouring voids aligned along crystallographic axes to grow while non-aligned voids will vanish.

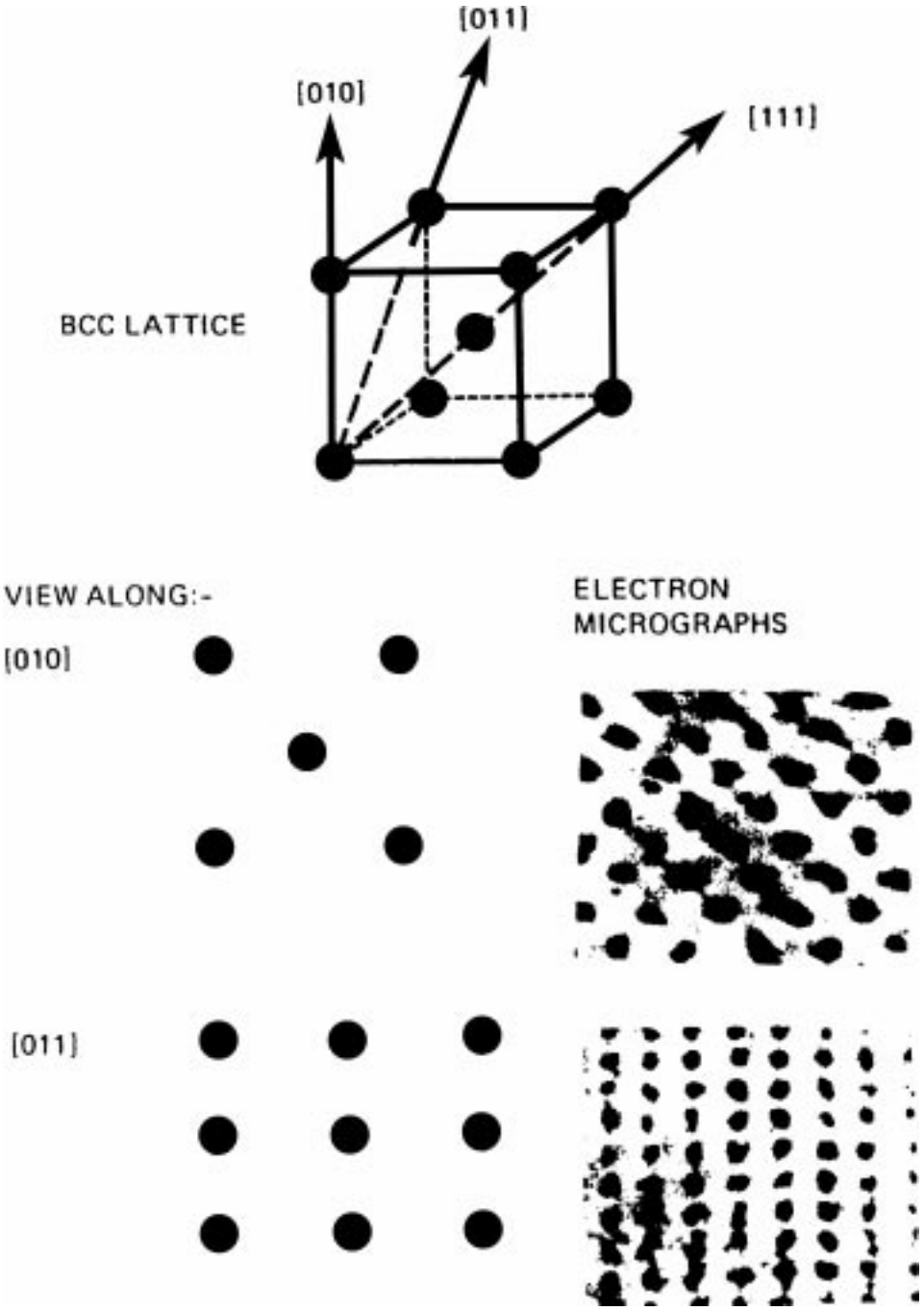

Figure 26: The projection of a *bcc* lattice along the [010] and [011] directions together with TEM micrographs of the corresponding void arrays in molybdenum after 2 MeV implantation of 10^{18} N^+ cm^{-2} at 950 ^{0}C. (From reference [198].)

V. Conclusion

After more than half a century of intensive research on radiation damage in metals, an overall picture on the general principals and mechanisms responsible for defect creation and defect dynamics has emerged. There are, however, some areas where a clear understanding of observed effects is still lacking.

One outstanding problem is revolving about the role different interstitial configurations play in annealing of electron irradiated metals at low temperatures. The question whether Stage I annealing is due to migration of crowdion or dumbbell type interstials is not yet finally answered, although the existence of static crowdions in most metals seems to be confirmed by computer simulations. Furthermore the observation that in some metals Stage IV annealing is missing needs an explanation. Is the reason behind it that in those metals the activation energies for migration of two different defects are fortuitously similar to each other, resulting in an overlap of Stages III and IV? If this is so, what type of defects are migrating at this temperature and have dumbbell interstials and vacancies comparable migration activation energies?

Another field where more information is needed is concerned with the occurrence of enhanced damage ranges in *fcc* metals after heavy ion implantation. According to the author's knowledge, no computer simulations have up to now been able to simulate this phenomenon. The question whether implanted ions produce shock waves, transporting sufficient energy into the bulk to produce dislocations at depths far beyond the ion's range, can probably only be answered by theorists applying appropriate models.

Finally, the explanation of the damage produced in many metals by electronic stopping of fast heavy ions is still controversial. Both the Thermal Spike Model and the Coulomb Explosion Model, provide plausible reasons for this effect. Probably both mechanisms are relevant with varying dominance — depending on the e-p coupling constant and thermodynamic properties of the particular metal involved.

Acknowledgment

Financial support from the National Research Foundation is gratefully acknowledged.

References

[1] **Thompson, M.W.,** Defects and Radiation Damage in Metals, Cambridge University Press, London, 1969.

[2] **Gibson, J.B., Goland, A.N., Milgram, M., and Vinyard, G.H.,** *Phys. Rev.*, 120, 1229, 1960.

[3] **Erginsoy, C., Vineyard, G.H., and Englert, A.,** *Phys. Rev.*, 133, A595, 1964.

[4] **Johnson, R.A.,** *Phys. Rev.*, 134, 1329, 1964.

[5] **Kawazoe, Y., Ohno, K., Shiga, K., Kamiyama, H., Tang, Z., Hasegawa, M., Matsui, H.,** *Nucl. Instr. and Meth.*, B153, 77, 1999.

[6] **Bacon, D.J.,** *J. Nucl. Mater.*, 159, 176, 1988.

[7] **Frank, W.,** *J. Nucl. Mater.,* 159, 122, 1988.

[8] **Johnson, R.A.,** *Phys. Rev.,* 145, 423, 1966.

[9] **Johnson, R.A. and Brown, E.,** *Phys. Rev.,* 127, 446, 1962.

[10] **Doyama, M. and Cotterill, R.M.J.,** *Phys. Rev.,* 137, A994, 1964.

[11] **Johnson, R.A.,** *Phys. Rev.,* 152, 629, 1966.

[12] **Bourret, A.,** *Phys. Stat. Sol. (a),* 4, 813, 1971.

[13] **Hossain, M.K. and Brown, L.M.,** *Radiat. Eff.,* 31, 203, 1977.

[14] **Wirth, B.D., Odette, G.R., Maroudas, D., and Lucas, G.E.,** *J. Nucl. Mater.,* 224, 185, 1997.

[15] **Itakura, M., Kaburaki, H., and Kusunoki, K.,** *Nucl. Instr. and Meth.,* B153, 122, 1999.

[16] **Bacon, D.J., Gao, F., and Osetsky, Y.N.,** *Nucl. Instr. and Meth.,* B153, 87, 1999.

[17] **Huntington, H.B. and Seitz, F.,** *Phys. Rev.,* 91, 1092, 1953.

[18] **Dominguez-Vázquez, J., Andribet, E.P., Pérez-Martin, A.M.C., and Jiménez-Rodriguez, J.J.,** *Surf. and Coatings Technology,* 83, 55, 1996.

[19] **Seitz, F.,** *Discuss. Faraday Soc.,* 5, 571, 1949.

[20] **Kenik, E.A. and Mitchell, T.E.,** *Phil. Mag.,* 32, 815, 1975.

[21] **Sosin, A.,** *Phys. Rev.,* 126, 1698, 1962.

[22] **Jan, R.V. and Seeger, A.,** *Phys. Stat. Sol.,* 3, 465, 1963.

[23] **Wollenberger, H. and Wurm, J.,** *Phys. Stat. Sol.,* 9, 601, 1965.

[24] **Tianmin, W., Yuexia, W., Baoyi, W., and Bo, L.,** *Nucl. Instr. and Meth.,* B153, 99, 1999.

[25] **Gettys, W.E.,** *Phys. Rev.,* 146, 480, 1966.

[26] **Bauer, W. and Sosin, A.,** *J. Appl. Phys.,* 35, 703, 1964.

[27] **Kamada, K., Kazumata, Y., and Suda, S.,** *Phys. Stat. Sol.,* 7, 231, 1964.

[28] **Sosin, A. and Garr, K.,** *Phys. Stat. Sol.,* 8, 481, 1965.

[29] **Jung, P., Chaplin, R.L., Fenzl, H.J., Reichelt, K., and Wombacher, P.,** *Phys. Rev.,* B8, 553, 1973.

[30] **Bauer, W., Anderman, A.I., and Sosin, A.,** *Phys. Rev.,* 185, 1965, 870.

[31] **Howe, L.M.,** *Phil. Mag.,* 22, 965, 1970.

[32] **Mitchell, T.E., Das, G., and Kenik, E.A.,** *Proc. Int. Conf. on the Fundamental Aspects of Radiation Damage in Metals,* Gatlinburg, USA, p. 73, 1975.

[33] **Lomer, J.N. and Pepper, M.,** *Phil. Mag.,* 16, 1119, 1964.

[34] **Maury, F., Biget, M., Vajda, P., Lucasson, A., and Lucasson, P.,** *Phys. Rev.,* B14, 5303, 1976.

[35] **Biget, M., Vajda, P., Lucasson, A., and Lucasson, P.,** *Radiat. Eff.,* 21, 229, 1974.

[36] **Jung, P. and Schilling, W.,** *Phys. Rev.,* B5, 2046, 1972.

[37] **Maury, F., Vajda, P., Lucasson, A., and Lucasson, P.,** *Phys. Rev.,* B8, 5496, 1973; *Phys. Rev.,* B8, 5506, 1973.

[38] **Vajda, P.,** *Rev. Mod. Phys.,* 49, 481, 1977.

[39] **Silsbee, R.H.,** *J. Appl. Phys.,* 28, 1246, 1957.

[40] **Leibfried, G.,** *J. Appl. Phys.,* 30, 1388, 1959.

[41] **Nelson, R.S. and Thompson, M.W.,** *Proc. Roy. Soc.,* A259, 458, 1961.

[42] **Leibfried, G. and Dederichs, P.H.,** *Z. Physik,* 170, 320, 1962.

[43] **Lehmann, C. and Leibfried, G.,** *Z. Physik,* 162, 203, 1961.

[44] **Anderson, H.H. and Sigmund, P.,** Danish Atomic Energy Commission, Risö Report No. 103, 1965.

[45] **Nelson, R.S.,** *Radiation Damage Processes in Materials,* ed. C.H.S. Dupuy, Noordhoff, Leyden, p. 261, 1975.

[46] **Averback, R.S., Benedek, R., and Merkle, K.L.,** *Phys. Rev.,* B18, 4156, 1978.

[47] **Seitz, F. and Koehler, J.S.,** *Solid State Phys.,* 2, 351, 1956.

[48] **Protasov, V.I. and Chudinov, V.G.,** *Radiat. Eff.,* 66, 1, 1982.

[49] **Kapinos, V.G. and Platonov, P.A.,** *Radiat. Eff.,* 103, 45, 1987.

[50] **Kinchin, G.H. and Pease, R.S.,** *Rep. Prog. Phys.,* 18, 1, 1955.

[51] **Robinson, M.T.,** *Phil. Mag.,* 12, 741, 1965.

[52] **Sigmund, P.,** *Radiat. Eff.,* 1, 15, 1969.

[53] **Norgett, M.J., Robinson, M.T., and Torrens, I.M.,** *Nucl. Eng. and Design,* 33, 50, 1975.

[54] **Chadderton, L.T.,** *Radiation Damage in Crystals,* Methuen's, London, 1965.

[55] **Jung, P.,** *J. Nucl. Mater.,* 117, 70, 1983.

[56] **Dinhut, J.F., Benhameur, F., and Riviére, J.P.,** *Nucl. Instr. and Meth.,* B71, 191, 1992.

[57] **Beeler Jr., J.R.,** *Phys. Rev.,* 150, 470, 1966.

[58] **Robinson, M.T. and Torrens, I.A.,** *Phys. Rev.,* 9B, 5008, 1974.

[59] **Benedek, R.,** *J. Appl. Phys.,* 52, 5557, 1981.

[60] **Robinson, M.T.,** *Nucl. Instr. and Meth.,* B67, 396, 1992.

[61] **Morioka, T., Morishita, K., and Sekimura, N.,** *Nucl. Instr. and Meth.,* B153, 130, 1999.

[62] **Ziegler, J.F., Biersack, J.P., and Littmark, U.,** *The Stopping and Ranges of Ions in Solids,* Pergamon Press, New York, 1985.

[63] **Andersen, H.H.,** *Nucl. Instr. and Meth.,* B18, 321, 1987.

[64] **Smith, R. and Webb, R.P.,** *Nucl. Instr. and Meth.,* B67, 373, 1992.

[65] **Diaz de la Rubia, T., Averback, R.S., Benedek, R., and King, W.E.,** *Phys. Rev. Lett.,* 59, 1930, 1987.

[66] **Brinkman, J.A.,** *J. Appl. Phys.,* 25, 961, 1954.

[67] **Averback, R.S., Diaz de la Rubia, T., Hsieh, H., and Benedek, R.,** *Nucl. Instr. and Meth.,* B59/60, 709, 1991.

[68] **Vineyard, G.H.,** *Radiat. Eff.,* 29, 245, 1976.

[69] **Hou, M. and Pan, Z.,** *Nucl. Instr. and Meth.,* B67, 401, 1992.

[70] **Soneda, N. and Diaz de la Rubia, T.,** *Phil. Mag.,* A78, 995, 1998.

[71] **Almazouzi, A., Caturla, M.J., Alluralde, M., Diaz de la Rubia, T., and Victoria, M.,** *Nucl. Instr. and Meth.,* B153, 105, 1999.

[72] **Brimhall, J.L. and Mastel, B.,** *J. Nucl. Mater.,* 29, 123, 1969.

[73] **Rau, R.C., Ladd, R.C., and Moteff, J.,** *J. Nucl. Mater.,* 33, 325, 1969.

[74] **Kulcinski, G.L., Mastel, B., and Brimhall, J.L.,** *Radiat. Eff.,* 2, 57, 1969.

[75] **Kulcinski, G.L. and Brimhall, J.L.,** *Phys. Stat. Sol. (a),* 5, K1, 1971.

[76] **Norris, D.I.R.,** *Radiat. Eff.,* 14, 1, 1972.

[77] **Norris, D.I.R.,** *Radiat. Eff.,* 15, 1, 1972.

[78] **Norris, D.I.R.,** *Nature,* 227, 830, 1970.

[79] **Norris, D.I.R.,** *Phil. Mag.,* 23, 135, 1971.

[80] **Norris, D.I.R.,** *Phys. Stat. Sol (a),* 4, K5, 1971.

[81] **Urban, K.,** *Phys. Stat. Sol (a),* 3 K167, 1970.

[82] **Sigler, J.A. and Kuhlmann-Wilsdorf, D.,** *Phys. Stat. Sol.,* 21, 545, 1967.

[83] **Brimhall, J.L. and Mastel, B.,** *Radiat. Eff.,* 3, 203, 1970.

[84] *Int. Symp. on Fundamental Aspects of Helium in Metals,* Jülich, Radiat. Eff. 78, 1, 1993.

[85] **Donnelly, S.E.,** *Radiat. Eff.,* 90, 1, 1985.

[86] **Kuzminov, D., Templier, C., Raqi, E., and Garem, H.,** *Nucl. Instr. and Meth.,* B72, 69, 1992.

[87] **Wilson, W.D.,** *Radiat. Eff.,* 78, 11, 1983.

[88] **Trinkaus, H.,** *Radiat. Eff.,* 78, 189, 1983.

[89] **Evans, J.H.,** *Nucl. Instr. and Meth.,* B18, 16, 1986.

[90] **Greenwood, G.W., Foreman, A.J.E., and Rimmer, D.E.,** *J. Nucl. Mater.,* 4, 305, 1959.

[91] **vom Felde, A., Fink, J., Müller-Heinzerling, Th., Pflüger, J., Scheerer, B., and Linker, G.,** *Phys. Rev. Lett.,* 53, 922, 1984.

[92] **Bethe, H. and Heitler, W.,** *Proc. R. Soc.,* A146, 83, 1934.

[93] **McKinley, W.A. and Feshbach, H.,** *Phys. Rev.,* 74, 1759, 1948.

[94] **Lindhard, J., Scharff, M., and Schiøtt, H.E.,** *Mat. Fys. Medd. Dan. Vid. Selsk.,* 33, no.14, 1963.

[95] **Lindhard, J. and Scharff, M.,** *Phys. Rev.,* 124, 128, 1961.

[96] **Bethe, H.,** *Ann. Physik,* 5, 324, 1930.

[97] **Bloch, F.,** *Z. Physik,* 81, 363, 1933.

[98] **Sigmund, P.,** *Rev. Roum. Phys.,* 17, 823, 1972.

[99] **Kumakhov, M.A. and Komarov, F.F.,** *Energy Loss and Ion Ranges in Solids,* Gordon & Breach, New York, 1981.

[100] **Nastasi, M., Mayer, J.W., and Hirvonen, J.K.,** *Ion-Solid Interactions: Fundamentals and Applications,* Cambridge University Press, Cambridge, 1996.

[101] **Sigmund, P.,** *Nucl. Instr. and Meth.,* B135, 1, 1998.

[102] **Feshbach, H., Porter, C.E., and Weisskopf, V.F.,** *Phys. Rev.,* 96, 448, 1954.

[103] **Rhein, W.J.,** *Phys. Rev.,* 98, 1300, 1955.

[104] **Coon, J.H., Davis, R.W., Felthauser, H.E., and Nicodemus, D.B.,** *Phys. Rev.,* 111, 250, 1958.

[105] **Meyer, O. and Turos, A.,** *Materials Science Reports 2,* 371, 1987.

[106] **Schilling, W., Burger, G., Isebeck, K., and Wenzl, H.,** *Vacancies and Interstitials in Metals,* Eds. Seeger, A., Schumacher, D., and Diehl, J., North-Holland, Amsterdam, p. 255, 1970.

[107] **Corbett, J.W.,** *Vacancies and Interstitials in Metals,* Eds. Seeger, A., Schumacher, D., Schilling, W., and Diehl, J., North Holland, Amsterdam, p. 977, 1970.

[108] **Seeger, A.,** *Vacancies and Interstitials in Metals,* Eds. Seeger, A., Schumacher, D., Schilling, W., and Diehl, J., North Holland, Amsterdam, p. 999, 1970.

[109] **Frank, W., Seeger, A., and Schottky, G.,** *Phys. Stat. Sol.*, 8, 345, 1965.

[110] **Koehler, J.S.,** *Vacancies and Interstitials in Metals*, Eds. Seeger, A., Schumacher, D., Schilling, W., and Diehl, J. North-Holland, Amsterdam, p. 989, 1970.

[111] **Seeger, A.,** *Physics Lett.*, A35, 135, 1971.

[112] **Decker, W., Diehl, J., Dunlop, A., Frank, W., Kronmüller, H., Mensch, W., Schaefer, H.E., Schwendemann, B., Seeger, A., Stark, H.P., Walz, F., and Weller, M.,** *Phys. Stat. Sol. (a)*, 52, 239, 1979.

[113] **Gilhaus, H. and Schüle, W.,** *Radiat. Eff. and Def. in Solids*, 138, 29, 1996.

[114] **W. Schüle,** *Z. Metallkd.*, 85, 78, 1994.

[115] **Leteurtre, J.,** *Site Characterization and Aggregation of Implanted Atoms in Materials*, Eds. Perez, A. and Coussement, R., Plenum Press, New York, p. 265, 1978.

[116] **Hood, G.M.,** *J. Nucl. Mater.*, 159, 149, 1988.

[117] **Brown, L.M., Kelly, A., and Mayer, R.M.,** *Phil. Mag.*, 19, 721, 1969.

[118] **Brown, L.M.,** *Phil. Mag.*, 19, 869, 1969.

[119] **Goringe, M.J.,** *Radiat. Eff.*, 10, 169, 1971.

[120] **Makin, M.J.,** *Phil. Mag.*, 18, 637, 1969.

[121] **Spring, M.S., Ipohorski, M., and Goringe, M.J.,** *Radiat. Eff.*, 11, 251, 1971.

[122] **Urban, K. and Seeger, A.,** *Phil. Mag.*, 30, 1395, 1974.

[123] **Davisson, C.M.,** *Alpha-, Beta- and Gamma-Ray Spectroscopy*, Ed. Siegbahn, K., North-Holland, Amsterdam, p. 37, 1966.

[124] **Coltman, R.R., Klabunde, C.E., and Redman, J.K.,** *Phys. Rev.*, B156, 715, 1966.

[125] **Isebeck, K. and Poole, K.F.,** *Radiat. Eff.*, 22, 15, 1974.

[126] **Burger, G., Meissner, H., and Schilling, W.,** *Phys. Stat. Sol.*, 4, 267, 1964.

[127] **Zinkle, S.J.,** *J. Nucl. Mater.*, 150, 140, 1987.

[128] **Coltman, R.R., Clabunde, C.E., McDonald, D.L., and Redman, J.K.,** *J. Appl. Phys.*, 33, 3509, 1962.

[129] **Nakagawa, M., Böning, K., Rosner, P., and Vogl, G.,** *Phys. Rev.*, B15, 5285, 1977.

[130] **Herschbach, K. and Jackson, J.J.,** *Phys. Rev.*, 153, 689, 1967.

[131] **Scapellato, N., Uhrmacher, M., and Lieb, K.P.,** *J. Phys. F*, 18, 677, 1988.

[132] **Keinonen, J., Kehrel, A., Lieb, K.P., and Uhrmacher, M.,** *Nucl. Instr. and Meth.*, B66, 209, 1992.

[133] **McKee, J.S.C., Mathur, M.S., and Smith, G.R.,** *Scanning Microscopy*, 7, 117, 1993.

[134] **Mathur, M.S., McKee, J.S.C., Liu, M., and He, D.,** *Mater. Sci. and Eng.*, B45, 25, 1997.

[135] **Magnuson, G.D., Palmer, W., and Koehler, J.S.,** *Phys. Rev.*, 109, 1990, 1958.

[136] **Granato, A.V. and Nilan, T.G.,** *Phys. Rev. Lett.*, 6, 171, 1961.

[137] **Herschbach, K. and Jackson, J.J.,** *Phys. Rev.*, 153, 694, 1967.

[138] **Herschbach, K. and Jackson, J.J.,** *Phys. Rev.*, 158, 661, 1967.

[139] **Averback, R.S. and Ghaly, M.,** *Nucl. Instr. and Meth.*, B127/128, 1, 1997.

[140] **Armour, D.G. and Al-Bayati, A.H.,** *Nucl. Instr. and Meth.*, B67, 279, 1992.

[141] **Matthews, L.M. and Ball, C.A.B.,** *J. Appl. Phys.*, 61, 2166, 1987.

[142] **Wiedersich, H.,** *Nucl. Instr. and Meth.*, B7/8, 1, 1985.

[143] **Seidman, D.N.,** *J. Phys. F: Metal Phys.*, 3, 393, 1973.

[144] **Stiller, K.,** *Radiat. Eff.*, 105, 53, 1987.

[145] **Current, M.I., Wei, C.-Y., and Seidman, D.N.,** *Phil. Mag.*, 43, 103, 1981.

[146] **Sato, S., Kohyama, A., and Igata, N.,** *Appl. Surf. Sci.*, 76/77, 285, 1994.

[147] **Pramanik, D. and Seidman, D.N.,** *Nucl. Instr. and Meth.*, 209/210, 453, 1983.

[148] **Bourdelle, K.K., Andersen, H.H., Johansen, A., Johnson, E., Sarholt-Kristensen, L., Steenstrup, S., and Yu, L.,** *Nucl. Instr. and Meth.*, B64, 143, 1992.

[149] **Wyser, A., Schäublin, R., and Gotthardt, R.,** *Nucl. Instr. and Meth.*, B107, 273, 1996.

[150] **Donnelly, S.E., Birtcher, R.C., and Templier, C.,** *Nucl. Instr. and Meth.*, B106, 583, 1995.

[151] **Walter, G., Heitzmann, R., Rück, D.M., Stahl, B., Gellert, R., Geiss, O., Klingelhöfer, G., and Kankeleit, E.,** *Nucl. Instr. and Meth.*, B113, 167, 1996.

[152] **Vos, M. and Boerma, D.O.,** *Nucl. Instr. and Meth.*, B15, 337, 1986.

[153] **Friedland, E., le Roux, H., and Malherbe, J.B.,** *Radiat. Eff.*, 87, 281, 1986.

[154] **Friedland, E. and Alberts, H.W.,** *Nucl. Instr. and Meth.*, B33, 710, 1988.

[155] **Friedland, E., van der Berg, N.G., Meyer, O., and Kalbitzer, S.,** *Nucl. Instr. and Meth.*, B118, 29, 1996.

[156] **Hertel, B.,** *Phil. Mag.*, A40, 331, 1979.

[157] **Friedland, E. and Alberts, H.W.,** *Nucl. Instr. and Meth.*, B35, 244, 1988.

[158] **Ecker, K.H., Macht, M.-P., and Naundorf, V.,** *Nucl. Instr. and Meth.*, B15, 66, 1986.

[159] **Friedland, E. and Fletcher, M.,** *Nucl. Instr. and Meth.*, B64, 242, 1992.

[160] **Sharkeev, Y.P., Girsova, N.V., Ryabcchikov, A.I., Kozlov, E.V., Perevalova, O.B., Brown, I.G., and Yao, X.Y.,** *Nucl. Instr. and Meth.*, B106, 532, 1995.

[161] **Friedland, E., van der Berg, N.G., Hanßmann, J., and Meyer, O.,** *Surf. Coatings and Technology*, 83, 10, 1996.

[162] **Averback, R.S., Diaz de la Rubia, T., and Benedek, R.,** *Nucl. Instr. and Meth.*, B33, 693, 1988.

[163] **Audouard, A., Balanzat, E., Bouffard, S., Jousset, J.C., Chamberod, A., Dunlop, A., Lesueur, D., Fuchs, G., Spohr, R., Vetter, J., and Thomé, L.,** *Phys. Rev. Lett.*, 65, 875, 1990.

[164] **Klaumünzer, S. and Schumacher, G.,** *Phys. Rev. Lett.*, 51, 1987, 1983.

[165] **Klaumünzer, S., Hou, M.-D., and Schumacher, G.,** *Phys. Rev. Lett.*, 57, 850, 1986.

[166] **Riviére, J.P., Dinhut, J.F., Paumier, E., and Dural, J.,** *Nucl. Instr. and Meth.*, B72, 176, 1992.

[167] **Dunlop, A., Lesueur, D., Morillo, J., Dural, J., Spohr, R., and Vetter, J.,** *Nucl. Instr. and Meth.*, B48, 419, 1990.

[168] **Dunlop, A., Legrand, P., Lesueur, D., Lorenzelli, N., Morillo, J., Barbu, A., and Bouffard, S.,** *Europhys. Lett.*, 15, 765, 1991.

[169] **Henry, J., Barbu, A., Leridon, B., Lesueur, D., and Dunlop, A.,** *Nucl. Instr. and Meth.*, B67, 390, 1992.

[170] **Dufour, C., Audouardt, A., Beuneu, F., Dural, J., Girard, J.P., Hairie, A., Levalois, M., Paumier, E., and Toulemonde, M.,** *J. Phys.: Condens. Matter*, 5, 4573, 1993.

[171] **Dunlop, A. and Lesueur, D.,** *Radiat. Eff. and Def. in Solids*, 126, 123, 1993.

[172] **Chimi, Y., Iwase, A., Ishikawa, N., Kuroda, N., and Kambara, T.,** *Nucl. Instr. and Meth.*, B164/165, 408, 2000.

[173] **Dimitrov, C., Dammak, H., Legrand, P., Dunlop, A., and Lesueur, D.,** *Radiat. Eff. and Def. in Solids*, 126, 115, 1993.

[174] **Dammak, H., Dunlop, A., and Lesueur, D.,** *Nucl. Instr. and Meth.*, B107, 204, 1996.

[175] **Trautmann, C., Dufour, C., Paumier, E., Spohr, R., and Toulemonde, M.,** *Nucl. Instr. and Meth.*, B107, 397, 1996.

[176] **Dunlop, A., Dammak, H., and Lesueur, D.,** *Nucl. Instr. and Meth.*, B112, 23, 1996.

[177] **Wang, Z.G., Dufour, C., Cabeau, B., Dural, J., Fuchs, G., Paumier, E., Pawlak, F., and Toulemonde, M.,** *Nucl. Instr. and Meth.*, B107, 175, 1996.

[178] **Klaumünzer, S., Li, C., Löffler, S., Rammensee, M., Schumacher, G., and Neitzert, H.C.,** *Rad. Eff. and Def. in Solids*, 108, 131, 1998.

[179] **Audouard, A., Balanzat, E., Jousset, J.C., Lesueur, D., and Thomé, L.,** *Radiat. Eff. and Def. in Solids,* 126, 93, 1993.

[180] **Benyagoub, A. and Klaumünzer, S.,** *Radiat. Eff. and Def. in Solids,* 126, 105, 1993.

[181] **Garrido, F., Benyagoub, A., Chamberod, A., Dran, J.C., Dunlop, A., Klaumünzer, S., and Thomé, L.,** *Radiat. Eff. and Def. in Solids,* 126, 129, 1993.

[182] **Gutzmann, A., Klaumünzer, S., Benyagoub, A., and Nagengast, D.,** *Radiat. Eff. and Def. in Solids,* 126, 133, 1993.

[183] **Benyagoub, A., Chamberod, A., Dran, J.C., Dunlop, A., Garrido, F., Klaumünzer, S., and Thomé, L.,** *Nucl. Instr. and Meth.,* B106, 500, 1995.

[184] **Benyagoub, A., Chamberod, A., Dran, J.C., Dunlop, A., Garrido, F., Klaumünzer, S., and Thomé, L.,** *Nucl. Instr. and Meth.,* B107, 189, 1996.

[185] **Audouard, A., Balanzat, E., Jousset, J.C., Chamberod, A., Fuchs, G., Lesueur, D. and Thomé, L.,** *Phil. Mag.,* B63, 727, 1991.

[186] **Dufour, C., Paumier, E., and Toulemonde, M.,** *Radiat. Eff. and Def. in Solids,* 126, 119, 1993.

[187] **Wang, Z.G., Dufour, C., Paumier, E., and Toulemonde, M.,** *J. Phys.: Condens. Matter,* 6, 6733, 1994.

[188] **Toulemonde, M., Dufour, C., Wang, Z., and Paumier, E.,** *Nucl. Instr. and Meth.,* B112, 26, 1996.

[189] **Dufour, C., Wang, Z.G., Levalois, M., Marie, P., Paumier, E., Pawlak, F., and Toulemonde, M.,** *Nucl. Instr. and Meth.,* B107, 218, 1996.

[190] **Volkov, A.E. and Borodin, V.A.,** *Nucl. Instr. and Meth.,* B107, 172, 1996.

[191] **Dufour, C., Paumier, E., and Toulemonde, M.,** *Nucl. Instr. and Meth.,* B122, 445, 1997.

[192] **Wang, Z.G., Dufour, C., Paumier, E., and Toulemonde, M.,** *Nucl. Instr. and Meth.,* B115, 577, 1996.

[193] **Yavlinskii, Y.N.,** *Nucl. Instr. and Meth.,* B115, 594, 1996.

[194] **Dammak, H., Lesueur, D., Dunlop, A., Legrand, P., and Morillo, J.,** *Radiat. Eff. and Def. in Solids,* 126, 111, 1993.

[195] **Legrand, P., Morillo, J., and Pontikis, V.,** *Radiat. Eff. and Def. in Solids,* 126, 151, 1993.

[196] **Lesueur, D. and Dunlop, A.,** *Radiat. Eff. and Def. in Solids,* 126, 163, 1993.

[197] **Ossi, P.M. and Pastorelli, R.,** *Nucl. Instr. and Meth.,* B122, 566, 1997.

[198] **Evans, J.H.,** *Radiat. Eff.,* 10, 55, 1971.

[199] **Evans, J.H., Bullough, R., and Stoneham, A.M.,** *Radiation-induced Voids in Metals,* Eds. Corbett, J.W. and Ianniello, L.C., US Atomic Commission, p. 522, 1972.

[200] **Jostsons, A. and Farrell, K.,** *Radiat. Eff.*, 15, 217, 1972.

[201] **Sass, S. and Eyre, B.L.,** *Phil. Mag.*, 27, 1447, 1973.

[202] **Johnson, P.B. and Mazey, D.J.,** *Radiat. Eff.*, 53, 195, 1980.

[203] **Jin, N.Y., Phillipp, F., and Seeger, A.,** *Phys. Stat. Sol. (a)*, 116, 91, 1989.

[204] **Jäger, W., Ehrhart, P. and Schilling, W.,** *Solid State Phenomena*, 3/4, 279, 1988.

[205] **Lück, G. and Sizmann, R.,** *Phys. Stat. Sol.*, 6, 263, 1964.

[206] **Lück, G. and Sizmann, R.,** *Phys. Stat. Sol.*, 14, 507, 1966.

[207] **Seeger, A.,** *Radiat. Eff. and Def. in Solids*, 111, 355, 1989.

[208] **Walgraef, D. and Ghoniem, N.M.,** *Phys. Rev.*, B52, 3951, 1995.

[209] **Woo, C.H. and Frank, W.,** *J. Nucl. Mater.*, 148, 121, 1987.

[210] **Frank, W., Hähner, P., Klemm, T., Tölg, C., and Zaiser, M.,** *Continuum Models and Discrete Systems*, Ed. Markov, K.Z., World Scientific Publishing Company, p. 412, 1996.